



1 **Unchanged PM_{2.5} levels over Europe during COVID-19 were**
2 **buffered by ammonia**

3

4 **Nikolaos Evangeliou^{1,*}, Ondřej Tichý², Marit Svendby Otervik¹, Sabine Eckhardt¹, Yves**
5 **Balkanski³, Didier Hauglustaine³**

6

7 ¹ NILU, Department for Atmospheric & Climate Research (ATMOS), 2007 Kjeller, Norway.

8 ² The Czech Academy of Sciences, Institute of Information Theory and Automation, Prague, Czech
9 Republic.

10 ³ Laboratoire des Sciences du Climat et de l'Environnement (LSCE), CEA-CNRS-UVSQ, 91191,
11 Gif-sur-Yvette, France.

12

13 * Corresponding author: N. Evangeliou (Nikolaos.Evangeliou@nilu.no)

14

15



16 **Abstract**

17 The coronavirus outbreak in 2020 had devastating impact on human life, albeit a positive effect
18 for the environment reducing emissions of primary aerosols and trace gases and improving air quality.
19 In this paper, we present inverse modelling estimates of ammonia emissions during the European
20 lockdowns of 2020 based on satellite observations. Ammonia has a strong seasonal cycle and mainly
21 originates from agriculture. We further show how changes in ammonia levels over Europe, in
22 conjunction with decreases in traffic-related atmospheric constituents modulated PM_{2.5}. The key
23 result of this study is a -9.8% decrease in emissions in the first half of 2020 compared to the same
24 period in 2016–2019 attributed to restrictions related to the global pandemic. We further calculate the
25 delay in the evolution of the emissions in 2020 before, during and after lockdowns, by an sophisticated
26 comparison of the evolution of ammonia emissions during the same time periods for the reference
27 years (2016–2019). Our analysis demonstrates a clear delay in the evolution of ammonia emissions
28 of -77 kt, that was mainly observed in the countries that suffered the strictest travel, social and
29 working measures. Despite the general drop in emissions during the first half of 2020 and the delay
30 in the evolution of the emissions during the lockdown period, satellite and ground-based observations
31 showed that European levels of ammonia increased. On one hand, this was due to the reduction of
32 SO_2 and NO_x (precursors of the atmospheric acids with which ammonia reacts) that caused less
33 binding and thus less chemical removal of ammonia (smaller loss – higher lifetime); on the other, the
34 majority of the emissions persisted, because ammonia mainly originates from agriculture, a primary
35 production sector that was not influenced by the lockdown restrictions, as practically agricultural
36 activity never ceased. Despite the projected drop in various atmospheric aerosols and trace gases,
37 PM_{2.5} levels stayed unchanged or even increased in Europe due to a number of reasons attributed to
38 the complicated $NH_3 - H_2SO_4 - HNO_3$ system. Higher water vapour during the European lockdowns
39 favoured more sulfate production from SO_2 and OH (gas phase) or O_3 (aqueous phase). Ammonia
40 first neutralised sulfuric acid (due to higher atmospheric abundance) also producing sulfate. Then,
41 the continuously accumulating free ammonia reacted with nitric acid shifting the equilibrium reaction
42 towards particulate nitrate. In high free ammonia atmospheric conditions such as those in Europe
43 during the 2020 lockdowns, a small reduction of NO_x levels drives faster oxidation toward nitrate and
44 slower deposition of total inorganic nitrate causing high secondary PM_{2.5} levels.

45



46 **1 Introduction**

47 Ammonia (NH₃), the most abundant gas, has played a vital role in the evolution of human
48 population through the Haber–Bosch process (Chen et al., 2019). However, today it is recognized to
49 have significant negative influence, not only for the environment (Stevens et al., 2010), but also for
50 human population (Cohen et al., 2017; Pope and Dockery, 2006) and the climate (De Vries et al., 2011).
51 As an alkaline molecule, ammonia regulates the pH of clouds, while its excessive atmospheric
52 deposition and terrestrial runoff affect natural reservoirs creating algae blooms and degrading water
53 quality (Camargo and Alonso, 2006; Krupa, 2003). When emitted to the atmosphere, it reacts with
54 the abundant sulfuric and nitric acids (Malm, 2004) forming sulfate, nitrate, and ammonium and
55 contributing up to 50% to the total aerosol mass (Anderson et al., 2003). The latter has implications
56 for human health (Gu et al., 2014) as aerosols penetrate the human respiratory system and accumulate
57 in the lungs (Pope III et al., 2002) causing premature mortality (Lelieveld et al., 2015). Furthermore,
58 through secondary aerosol formation (Pozzer et al., 2017), ammonia has a significant impact (i) on
59 regional climate (Bellouin et al., 2011) causing visibility problems and contributing to haze effect,
60 and (ii) on global climate directly by scattering incoming radiation (Henze et al., 2012) and indirectly
61 as cloud condensation nuclei (Abbatt et al., 2006) altering the Earth’s radiative balance.

62 The largest portion of atmospheric ammonia originates from the synthesis of nitrogen
63 fertilizers, which are in high demand for agriculture (Erisman et al., 2007). The expansion of intensive
64 agriculture during the 20th century has increased atmospheric ammonia above natural levels (Erisman
65 et al., 2008), while the projected growth of the global population will likely create larger nutritional
66 needs that are expected to further increase ammonia emissions during the 21st century (Pai et al.,
67 2021). Other sources of ammonia include emissions from livestock (Sutton et al., 2000a), industry,
68 ammonia-rich watersheds (Sørensen et al., 2003), traffic (Kean et al., 2009), sewage (Reche et al.,
69 2012), humans (Sutton et al., 2000b), biomass and domestic combustion (Sutton et al., 2008; Fowler
70 et al., 2004) and volcanic eruptions (Sutton et al., 2008).

71 In the past years, atmospheric ammonia observations were mostly limited to ground-based
72 measurements with relatively sparse monitoring networks. This resulted in large emission
73 uncertainties in regions poorly covered by measurements (Heald et al., 2012). Today, satellite
74 products are capable to record daily ammonia column concentrations providing useful information
75 on its atmospheric abundance. Recently, Van Damme et al. (2021) analyzed Infrared Atmospheric
76 Sounding Interferometer (IASI) retrievals and showed increased ammonia levels over most of Europe
77 after 2015. Then, suddenly the COVID-19 outbreak came in 2020 creating a unique situation
78 (Baekgaard et al., 2020), which affected all segments of life in a detrimental way (Chakraborty and
79 Maity, 2020; Sohrabi et al., 2020). As a measure to inhibit further spread of the virus, authorities took



80 strict social, travel and working restrictions for months, which resulted in lower traffic-related
81 emissions and improved air quality (Bauwens et al., 2020; Dutheil et al., 2020; Sicard et al., 2020).
82 Illustrating the impact on emissions, Guevara et al. (2021) reported average emission reductions in
83 Europe to be 33% for NO_x , 8% for non-methane volatile organic compounds (NMVOCs), and 7%
84 for SO_x during the strictest lockdowns in 2020, while more than 85% of the total reduction is
85 attributed to road transport. CO_2 emissions were also decreased by 11% over Europe during the first
86 lockdowns (Diffenbaugh et al., 2020), so as aerosols did; notably Black Carbon (BC) emissions
87 dropped by 11% (Evangelidou et al., 2020) and Aerosol Optical Depth (AOD) decreased up to 20%
88 over Central and Northern Europe (Acharya et al., 2021).

89 While the COVID-19 lockdown impact on emissions for primary aerosols and trace gases has
90 been studied extensively, how ammonia emissions were affected in Europe is unknown. The latter is
91 very important and may have largely moderated the atmospheric levels of particulate matter (Giani
92 et al., 2020; Guevara et al., 2021; Matthias et al., 2021), because of ammonia's contribution to
93 secondary $PM_{2.5}$ (particulate matter) formation (Anderson et al., 2003). Here, we make use of
94 satellite measurements of ammonia and a novel inversion algorithm to track how ammonia emissions
95 changed before, during and after the European lockdowns in 2020. We examine the reasons behind
96 the estimated changes and validate the results against ground-based observations from the EMEP
97 measurement network (<https://emep.int/mscw/>, **Figure S I**). Finally, we calculate the resulting impact
98 of ammonia changes during the European lockdowns on the formation of $PM_{2.5}$ using a chemistry
99 transport model (CTM) and try to interpret the mechanisms governing these changes.

100 2 Methods

101 2.1 Cross-Track Infrared Sounder (CrIS) ammonia measurements

102 The CrIS sensor onboard the NASA Suomi National Polar-orbiting Partnership provides
103 atmospheric soundings at high spectral resolution (0.625 cm^{-1}) (Shephard et al., 2015) resulting in
104 improved vertical sensitivity for ammonia at the surface (Zavyalov et al., 2013). The CrIS fast
105 physical algorithm (Shephard and Cady-Pereira, 2015) retrieves ammonia at 14 vertical levels using
106 a physics-based optimal estimation retrieval, which also provides the vertical sensitivity (averaging
107 kernels) and an estimate of the retrieval errors (error covariance matrices) for each measurement.
108 Shephard et al. (2020) reports a total column random measurement error of 10–15%, with total
109 random errors of ~30%. The individual profile random errors are 10–30%, while total profile random
110 errors increase above 60% due to the limited vertical resolution (Shephard et al., 2020). Vertical
111 sensitivity and error calculations are also important when using CrIS observations in satellite inverse
112 modelling applications (Li et al., 2019; Cao et al., 2020) as a satellite observational operator can be



113 generated in a robust manner (see next sections). The detection limit of CrIS measurements has been
114 calculated down to 0.3–0.5 ppbv (Shephard et al., 2020) and the product has been validated
115 extensively against ground-based observations (Dammers et al., 2017; Kharol et al., 2018) showing
116 small differences and high correlations.

117 Daily CrIS ammonia satellite measurements (version 1.6.2) were gridded on $0.5^\circ \times 0.5^\circ$ covering
118 all Europe (10°W – 50°E , 25°N – 75°N) from 1st January to 30th June 2020. Gridding was chosen to
119 limit the large number of observations (around 10,000 per day per vertical level for 2550 retrievals
120 January to June 2020), hence the need for a large number of source-receptor matrices (SRMs), which
121 is computationally inefficient. Specifically, day and night-time observations from CrIS were averaged
122 in each 0.5° resolution grid-cell daily from 1st January to 30th June 2020. This gridding method,
123 although simple, it gives more robust results than classic interpolation methods and presents small
124 standard deviations of the gridded values (see Tichý et al., 2023). Sitwell and Shephard (2021)
125 showed that the averaging kernels of CrIS ammonia are significant only for the lowest six levels (the
126 upper eight have no influence into the satellite observations) and therefore we have considered these
127 six vertical levels (~ 1018 – 619 hPa).

128 2.2 Source-receptor matrix (SRM) calculations

129 SRMs were calculated for each $0.5^\circ \times 0.5^\circ$ grid-cell over Europe (10°W – 50°E , 25°N – 75°N)
130 using the Lagrangian particle dispersion model FLEXPART version 10.4 (Pisso et al., 2019) adapted
131 to model ammonia. The model releases computational particles that are tracked backward in time
132 using hourly ERA5 (Hersbach et al., 2020) assimilated meteorological analyses from the European
133 Centre for Medium-Range Weather Forecasts (ECMWF) with 137 vertical layers and a horizontal
134 resolution of $0.5^\circ \times 0.5^\circ$. FLEXPART simulates turbulence (Cassiani et al., 2014), unresolved
135 mesoscale motions (Stohl et al., 2005) and convection (Forster et al., 2007). SRMs were calculated
136 for 7 days backward in time, at temporal intervals that matched satellite measurements and at spatial
137 resolution of $0.5^\circ \times 0.5^\circ$. This 7-day backward tracking is sufficiently long to include almost all
138 ammonia sources that contribute to surface concentrations at the receptors given a typical atmospheric
139 lifetime of about a day (Evangelou et al., 2021; Van Damme et al., 2018).

140 The complicated heterogeneous chemistry of ammonia was modelled with the Eulerian model
141 LMDz-OR-INCA, which couples the LMDz (Laboratoire de Météorologie Dynamique) General
142 Circulation Model (GCM) (Hourdin et al., 2006) with the INCA (INteraction with Chemistry and
143 Aerosols) model (Folberth et al., 2006; Hauglustaine et al., 2004) and with the land surface dynamical
144 vegetation model ORCHIDEE (ORganizing Carbon and Hydrology In Dynamic Ecosystems)
145 (Krinner et al., 2005). The model has a horizontal resolution of $2.5^\circ \times 1.3^\circ$, and 39 hybrid vertical
146 levels extending to the stratosphere. It accounts for large-scale advection of tracers (Hourdin and



147 Armengaud, 1999), deep convection (Emanuel, 1991), while turbulent mixing in the planetary
148 boundary layer (PBL) is based on a local second-order closure formalism. The model simulates
149 atmospheric transport of natural and anthropogenic aerosols and accounts for emissions, transport
150 (resolved and sub-grid scale), and dry and wet (in-cloud/below-cloud scavenging) deposition of
151 chemical species and aerosols interactively. LMDz-OR-INCA includes a full chemical scheme for
152 the ammonia cycle and nitrate particle formation, as well as a state-of-the-art
153 CH₄/NO_x/CO/NMHC/O₃ tropospheric photochemistry (Hauglustaine et al., 2014). The global
154 transport of ammonia was simulated for 2020 with a month of spin-up by nudging the winds of the
155 3-hourly ERA5 (Hersbach et al., 2020) with a relaxation time of 10 days (Hourdin et al., 2006).

156 For the calculation of ammonia's lifetime, LMDz-OR-INCA ran with traditional emissions for
157 anthropogenic, biomass burning and oceanic emission sources from ECLIPSEv5 (Evaluating the
158 CLimate and Air Quality ImPacts of Short-livEd Pollutants), GFED4 (Global Fire Emission Dataset)
159 and GEIA (Global Emissions InitiAtive) (hereafter called "EGG") (Bouwman et al., 1997; Giglio et
160 al., 2013; Klimont et al., 2017). FLEXPART uses the exponential mass removal for radioactive
161 species based on the e-folding lifetime (Pisso et al., 2019), which gives the time needed to reduce the
162 species mass to 1/e contribution. We calculated the e-folding lifetime (Kristiansen et al., 2016; Croft
163 et al., 2014) of ammonia from LMDz-OR-INCA, assuming that the loss occurs as a result of all
164 processes affecting ammonia (chemical reactions, deposition) with a minimum time-step of 1800 s.
165 Then we calculated the exponential loss of ammonia and the respective loss-rate constant κ (s⁻¹). We
166 point to Tichý et al. (2023) for more details on the methodology to avoid repetition.

167 Ammonia has a complicated atmospheric chemistry and may react with sulfuric and nitric acid
168 producing sulfate and nitrate. However, under certain atmospheric conditions, the equilibrium
169 reaction with nitric acid can be shifted to the left producing free ammonia (Seinfeld and Pandis, 2000).
170 Tichý et al. (2023) showed that production of free ammonia happened very rarely in continental
171 Europe in 2013–2020 period. Nevertheless, we have previously published a full validation of the
172 obtained CTM concentrations against all the available ground-based measurements of ammonia
173 globally (Tichý et al., 2023), from the EMEP network (<https://emep.int/mscw/>) in Europe, EANET
174 (East Asia acid deposition NETwork) in Southeastern Asia (<https://www.eanet.asia/>) and AMoN
175 (Ammonia Monitoring Network in the US, AMoN-US; National Air Pollution Surveillance Program
176 (NAPS) sites in Canada) in North America (<http://nadp.slh.wisc.edu/data/AMoN/>).

177 **2.3 Inverse modelling of ammonia emissions**

178 The proposed inversion method is based on a comparison of the CrIS satellite observations with
179 the model profile retrievals to estimate the spatiotemporal ammonia emissions. The comparison of
180 remote-sense observations such as CrIS with model (or in-situ) profiles is not straightforward as in



181 the cases of ground-based observations. Here, we used the more rigorous approach of the “instrument
182 operator” (see equation below), after interpolation of the model profile to the first six levels of the
183 satellite product (Rodgers, 2000):

$$184 \quad \ln(v^{ret}) = \ln(v^a) + A(\ln(v^{true}) - \ln(v^a)) \quad Eq. 1$$

185 where v^{ret} is the retrieved profile concentration vector, v^a is a priori profile concentration vector,
186 v^{true} is the true profile concentration vector, and A is the averaging kernel matrix in logarithmic
187 space (for each $0.5^\circ \times 0.5^\circ$ resolution grid-cell). In our inversion setup, we directly compared the
188 retrieved v^{ret} and the observed satellite column concentration v^{sat} that is given by CrIS. In our case,
189 v^{true} is equal to the modelled concentration v^{mod} calculated from the SRMs and a prior emission
190 inventory. The argument for this approach is that v^{ret} is what the satellite would observe if v^{mod} was
191 the true profile. This is a useful technique for evaluating if the retrieval algorithm is performing as
192 designed, i.e., is it unbiased and the calculated root mean square error (RMSE) is within the expected
193 variability. Further details about the algorithm and the setup can be found in Tichý et al. (2023).

194 The goal of the inversion is to iteratively update prior emissions by minimizing the distance
195 between v^{sat} and v^{ret} by correcting the emission flux x in the term $v^{mod} = srm^{Flex} x^a$ (srm^{Flex}
196 denotes the FLEXPART SRMs), at each grid-cell and each of the six vertical levels that are important
197 for CrIS (Sitwell et al., 2022):

$$198 \quad \arg \min_{x^a \rightarrow x} \|v^{sat} - v^{ret}\|_2^2 \quad Eq. 2$$

199 The inverse problem is constructed for each spatial element of the computational domain.
200 Inspired by the construction of covariance matrix in Cao et al. (2020), we consider 4° surroundings
201 (445 km), expressed by the index set \mathbb{S} , of which the column concentrations are considered due to
202 computational effectivity. Note that we observed low sensitivity of resulting emission estimates to
203 this choice. Then, we can formulate the inverse problem for each spatial element as:

$$204 \quad [v_{s_i}^{sat}; s_i \in \mathbb{S}] = [v_{s_i}^{ret}; s_i \in \mathbb{S}] q^{\mathbb{S}} \quad Eq. 3$$

205 where the left side of the equation is formed by the vector with aggregated CrIS observations, vectors
206 $v_{s_i}^{ret}$ form a block-diagonal matrix, and $q^{\mathbb{S}}$ is an unknown vector with correction coefficients for each
207 temporal element of the emission. The inverse problem in Eq. 3 was solved using the least squares
208 with adaptive prior covariance (LS-APC) algorithm (Tichý et al., 2016). The algorithm is based on a
209 Bayesian model which assumes that all coefficients are positive and that the abrupt changes in their
210 neighbouring values are less probable. It is shown that the method is less sensible to manual tuning
211 of regularization parameters (see sensitivity tests in Tichý et al. (2020)) than classical optimization



212 procedures, which is crucial for such a large dataset where each spatial element represents a separate
213 inverse problem.

214 A detailed description of the algorithm is given in Tichý et al. (2016). Here, we do not describe
215 the algorithm again but explain a few modifications that were necessary for this study. By estimating
216 the correction coefficients q^S for each grid-cell of the spatial domain (10°W–50°E, 25°N–75°N), we
217 can propagate the coefficients through Eq. 2 to update a priori emissions x^a in the model
218 concentration term v^{mod} . We follow Li et al. (2019) and Cao et al. (2020) to bound the ratio between
219 the prior and the posterior emissions. The lower and upper bound of this ratio is set to 0.01 and 100,
220 respectively, to omit the unrealistically low or high emissions. We consider these bounds large
221 enough to allow for new emission sources to be exposed, not presented in the prior emissions.

222 We evaluate the performance of the inversion by using three a priori emission datasets, (i) one
223 based on Van Damme et al. (2018) calculations (Evangelidou et al., 2021) (hereafter denoted as “VD”),
224 (ii) the ECLIPSEv6 inventory (Klimont, 2022; Klimont et al., 2017) (combined with biomass burning
225 emissions from GFEDv4 (Giglio et al., 2013)) as the most recent one (denoted as “EC6G4”), and (iii)
226 the average of four emission inventories for ammonia, except for these two mentioned before, “EGG”
227 (see previous section), and “NE” calculated from IASI (Infrared Atmospheric Sounding
228 Interferometer) observation (Evangelidou et al., 2021) (denoted as “avgEENV”). To account for the
229 spatiotemporal impact of the lockdown on the European emissions, we corrected prior emission
230 inventories of ammonia (EGG, EC6G4 and avgEENV) for 2020 using adjustment factors (AFs)
231 adopted from Doumbia et al. (2021). The same was done for SO_2 and NO_x (precursors of sulfuric and
232 nitric acid in the atmosphere) in EGG that was used to calculate ammonia’s loss rates using LMDz-
233 OR-INCA model (see section 2.2). This dataset provides, for the January–August 2020 period,
234 gridded AFs at a $0.1^\circ \times 0.1^\circ$ resolution on a daily resolution for transportation (road, air and ship
235 traffic), power generation, industry and residential sectors. The quantification of AFs is based on
236 activity data collected from different databases and previously published studies. These emission AFs
237 have been applied to the CAMS global inventory, and the changes in emissions of the main pollutants
238 have been assessed for different regions of the world in the first 6 months of 2020 (Doumbia et al.,
239 2021).

240 **Figure 1** shows the comparison of prior and posterior concentrations against independent
241 observations (observations that were not used in the inversion algorithm) from the EMEP network
242 (<https://emep.int/mscw/>, **Figure S 1**) for January–July 2020. Note that prior concentrations of
243 ammonia result by coupling the FLEXPART SRMs with prior emissions (from VD, ECLIPSEv6 and
244 avgEENV), while posterior concentrations by coupling the SRMs with the calculated posterior
245 emissions. In **Figure 1** it is evident that the most accurate reconstruction of surface concentrations



246 with respect to the EMEP observations was obtained using avgEENV as the a priori information, and
247 therefore the results presented hereafter are based on this setup. We performed inversions for the first
248 half of 2020 to assess the effect of lockdown measures on ammonia emissions, as well as the situation
249 after lockdown measures were taken away (rebound period). To have a more generic view, we also
250 performed inverse modelling calculations for the first half of each year between 2016–2019 (reference
251 period). Then, we assess in impact of ammonia changes on aerosol formation (PM_{2.5}), by feeding
252 the posterior emissions to the LMDz-OR-INCA model and calculating the production of PM_{2.5}.

253 2.4 Statistical tests

254 To evaluate the comparisons between modelled and observed concentrations of ammonia, we
255 used the root mean squared logarithmic error (RMSLE) defined as follows:

$$256 \quad RMSE = \sqrt{\frac{\sum_{i=1}^N (C_m - C_o)^2}{N}} \quad \text{and} \quad RMSLE = \sqrt{\frac{1}{N} \sum_{i=1}^N (\log C_m - \log C_o)^2} \quad Eq. 4$$

257 where C_m and C_o are the modelled and measured ammonia concentrations and N is the total number
258 of observations. The commonly used squared Pearson correlation coefficient (r) was also used as a
259 measure of linear correlation between two sets of data defined as:

$$260 \quad r = \frac{\sum (C_m - \bar{C}_m)(C_o - \bar{C}_o)}{\sqrt{(\sum (C_m - \bar{C}_m)^2)(\sum (C_o - \bar{C}_o)^2)}} \quad Eq. 5$$

261 where the distance of modelled and measured ammonia concentrations from the mean (\bar{C}_m and \bar{C}_o) is
262 computed. Finally, the standard deviation was adopted as a measure of the dispersion of modelled
263 ammonia from the observations, which is the true value:

$$264 \quad \sigma = \sqrt{\frac{\sum (C_m - C_o)^2}{N}} \quad Eq. 6$$

265 The mean fractional bias (MFB) was selected as a symmetric performance indicator that gives equal
266 weights to under- or over-estimated concentrations (minimum to maximum values range from -200%
267 to 200%). It was used in the independent validation (validation against measurements that were
268 excluded from the inversion, see section 3.2) of the posterior concentrations of ammonia during the
269 European lockdowns of 2020 and is defined as:

$$270 \quad MFB = \frac{1}{N} \frac{\sum_{i=1}^N (C_m - C_o)}{\sum_{i=1}^N \frac{(C_m + C_o)}{2}} \quad Eq. 7$$

271 For the same reason, the mean absolute error was computed normalized ($nMAE$) over the average of
272 all the actual values (observations here), which is a widely used simple measure of error:

$$273 \quad MAE = \frac{\sum_{i=1}^N |C_m - C_o|}{\sum_{i=1}^N C_o} \quad Eq. 8$$



274 3 Results

275 3.1 Emission changes of ammonia due to COVID-19 restrictions over Europe

276 The reason behind the selected three priors used in the inversion (EGG, EC6G4 and avgEENV)
277 of ammonia is trifold; (i) they are based on the most recent estimates, (ii) they present different spatial
278 distribution, and (iii) they were derived using different methodologies. More specifically, EC6G4 is
279 based on the emission model GAINS (Klimont et al., 2017), while VD uses satellite observations
280 combined with a box model (Evangelidou et al., 2021). As mentioned in the previous section, it is seen
281 that the most accurate representation of surface model concentrations was achieved using the
282 avgEENV a priori, which forces posterior concentrations closer to 1×1 line, whereas the obtained
283 statistics are significantly better than using other priors (**Figure 1**). Therefore, the results presented
284 below have all been obtained using avgEENV as the prior emission dataset keeping results using the
285 other two priors in the Supplements.

286 The total prior emissions of ammonia over Europe for the inversion period (January – June),
287 the posterior emissions for years 2016–2019 and the posterior emissions during the lockdown year
288 2020 (January – June) are plotted in **Figure 2** (the results from inversions using EC6G4 and VD prior
289 emissions are illustrated in **Figure S 2** and **S 3**). The total prior ammonia emitted between January
290 and June in Europe were equal to 1061 kt (**Figure 2a**). To check whether calculated changes in 2020
291 were due to meteorology and avoid misinterpretation of our findings, inverse calculations of ammonia
292 were performed for the reference years 2016–2019 (January–June) using respective observations
293 from CrIS and exactly the same set-up as the one described in section 2 (Methods). The total posterior
294 emissions of ammonia over Europe for the reference period (2016 – 2019) were estimated to be 1665
295 kt or 57% higher than the prior (**Figure 2b**). Finally, for January–June 2020 the derived emission
296 estimates were equal to 1568 kt (**Figure 2c**). This is 48% higher than the prior and 6% lower than the
297 posterior emissions of January–June 2016–2019.

298 The weekly-average evolution of prior and posterior emissions of ammonia over Europe
299 (January to June) for 2016–2019 show a similar pattern with small year-to-year variability (**Figure**
300 **2d,e**), thus insignificant impact from the prevailing meteorology. The weekly posterior ammonia
301 emissions over Europe changed during the lockdown period (2020) as compared to the reference
302 years (**Figure 2f**). Satellites and national monitoring measurements of ammonia show that emissions
303 peak in spring (March) and late-summer in Europe (Van Damme et al., 2022) corresponding to the
304 two main fertilization periods (Paulot et al., 2014). Ammonia abundances are however high
305 throughout the entire spring–summer period due to agricultural activities and temperature dependent
306 volatilization of ammonia (Sutton et al., 2013). Ammonia posterior emissions in 2020 declined by -



307 9.8% as compared to the same period over the previous four years (2016–2019, **Figure 2f**).
308 Interestingly, the posterior ammonia emissions in the first half of 2020 were insensitive to the
309 meteorological conditions. Although the obtained posterior emissions for the reference period are
310 very similar with respect to annual variance (grey shade in **Figure 2f**), levels and trend (dashed grey
311 line), emissions during lockdown period in 2020 dropped substantially, outside of the variance of
312 emissions calculated for the reference period (bottom blue line, **Figure 2f**).

313 **3.2 Validation of posterior ammonia against independent measurements**

314 The optimized emissions of ammonia must be validated against independent observations,
315 because the inversion algorithm has been designed to reduce the model–observation mismatches.
316 Here, the reduction of the posterior concentration differences from the observations from CrIS is
317 determined by the weighting that is given to the observations and, hence, such comparison depends
318 on this weighting (dependent observations). Therefore, the ideal comparison of any posterior
319 emission resulting from top-down methods would be against measurements that were not included in
320 the inversion algorithm (independent observations). Here, we used ground-based observations of
321 ammonia from all EMEP sites (<https://emep.int/mscw/>) for the period of our study as an independent
322 dataset for validation. All stations are illustrated in **Figure S 1**.

323 As we mentioned in section 2.3, we evaluated the efficiency of the inversion and the most
324 effective a priori dataset for our purpose by assessing the match between the calculated posterior
325 concentrations against all the available observations from EMEP (N=3957) for the study period
326 (**Figure 1**). More specifically, after it became evident that the most accurate results were obtained
327 with avgEENV as the prior (relationship closer to unity against measured ammonia), we saw an
328 immediate improvement in the statistical tests used (nRMSE, nMAE and RMSLE) when using the
329 posterior emissions to model ammonia in FLEXPART during the first half of 2020 (**Figure 1** – right
330 panel). nMAE decreased from 0.80 using the prior emissions to 0.76 using the posterior ones,
331 accordingly nRMSE of the posterior concentrations dropped to 0.073 as compared to -0.069 using
332 the prior emissions, while the RMSLE decreased from 0.60 using prior emissions to 0.55 using the
333 optimized a posteriori emissions. To get a better insight on how modelled concentrations improved
334 towards ammonia observations, eight random EMEP stations were selected to show timeseries of
335 prior and posterior concentrations in the first half of 2020 (**Figure S 4**). Although large peaks are not
336 reproduced, all statistics were improved using the posterior emissions of ammonia.

337 **3.3 Country-level changes due to COVID-19 restrictions**

338 To document the emission changes of ammonia over the different European countries before,
339 during and after the 2020 lockdowns, we report the weekly evolution of the emissions for 16 countries
340 individually (**Figure 3**). Specifically, weekly emissions were averaged for each country based on



341 respective country definitions that are shown in **Figure S 5**. Like in the previous section, the country-
342 based emissions were calculated for the avgEENV prior.

343 Most countries show that ammonia emissions declined or at least stayed less affected by the
344 2020 lockdowns, as compared to the same period during the reference years (2016–2019). Countries
345 with substantial decreases in the 2020 lockdown emissions were The Netherlands (-16%) and
346 Belgium (-23%), both countries with important agricultural activity, as well as Denmark (-20%),
347 Ireland (-18%) and Ukraine (-18%). Smaller changes were recorded in Spain (-2.1%), Czechia (-
348 4.0%) and Italy (-6.0%) despite the intensive lockdown measures. This practically shows that
349 agricultural activity never stopped, even in periods of extraordinary austerity, as agriculture is the last
350 remaining primary production sector, necessary for human life.

351 We note that the largest emissions of ammonia in European countries were seen around
352 March–April (weeks 8–16) and in summer. These coincide with the fertilization periods mentioned
353 previously (Paulot et al., 2014) that control the seasonality of ammonia’s emissions. In most European
354 countries, the time of the year when fertilizers can be applied is tightly regulated (Ge et al., 2020). In
355 the Netherlands for instance, the largest ammonia contributor in Europe, application of nitrogen
356 fertilizer is only allowed from February to mid-September. This produces two peak periods, in March
357 and late May (**Figure 3**). Manure application also follows stringent regulations and is only allowed
358 in the same periods depending on the type of manure (slurry or solid) and the type of land (grassland
359 or arable land) (Van Damme et al., 2022). In Belgium, nitrogen fertilizers are only allowed between
360 mid-February and end of August (Van Damme et al., 2022), therefore the peaks in early March and
361 summer (**Figure 3**). Accordingly, in Germany, it is also restricted in winter months and depends on
362 fertilizer type and land type (Kuhn, 2017), while restrictions during the same months are applied in
363 the US (Paulot et al., 2014).

364 To understand and position where ammonia emissions changed during the European
365 lockdowns of 2020, we plot the difference of the posterior emissions of ammonia during the lockdown
366 period (15 March – 30 April) for the same period in **Figure 4a**. We calculate higher emissions of
367 ammonia during the lockdown of +115 kt as compared to the prior emissions. The largest differences
368 can be seen in Spain, Romania and North Italy. Note that inversion algorithms aim at reducing the
369 mismatches between modelled concentrations and observations (in our case, from CrIS satellite
370 measurements) by correcting emissions. This means that different posterior emissions are most likely,
371 due to errors in the prior emissions and do not indicate any impact from the restriction measures.

372 Therefore, we demonstrate the impact of the COVID-19 lockdowns over Europe in 2020, by
373 calculating the emission anomaly for the lockdown period from 2016–2020 (same period as the 2020



374 lockdowns, namely 15 March – 30 April) in **Figure 4b**. Emissions during the 2020 lockdowns
375 dropped by -29 kt with respect to the same period in 2016 – 2020 showing the impact of the COVID-
376 19 restrictions. Maximum decreases were seen in The Netherlands and Belgium, both countries with
377 important agricultural activity (**Figure 4b**) that also suffered heavily from the COVID-19 outbreak
378 (Bendz and Aaberge, 2020) and took strict lockdown measures. Other areas where changes were
379 calculated were Northern Italy, Switzerland and Austria, while Scandinavian countries were not
380 affected. This agrees well with the state of the epidemic in these countries in spring 2020. While
381 North Italy was the first country outside China to suffer high mortality rates and, thus, dramatic social
382 restrictions in spring 2020, Norway, Sweden, Denmark and Finland showed total infected cases far
383 below 1% per capita, mostly suffering higher rates later in 2020 (Gordon et al., 2021).

384 It is well-known that ammonia emissions increase in spring (March) and late-summer in
385 Europe (Van Damme et al., 2022) corresponding to the two main fertilization periods (Paulot et al.,
386 2014) and that atmospheric abundances are high throughout the entire spring–summer period due to
387 agricultural activities and temperature dependent volatilization (Sutton et al., 2013). Therefore,
388 calculating the difference in the calculated emissions during the lockdown from the period before or
389 after is practically meaningless and cannot show the lockdown impact since agricultural activity did
390 not stop in spring 2020. For this reason we quantify the delay in the evolution of the emissions by
391 calculating emission differences in the lockdowns from the period before (Lock – Prelock) for the
392 lockdown year 2020 and emission differences (Lock – Prelock) for the reference years (2016 – 2019);
393 Then, we plot their spatial differences in **Figure 4c**. Accordingly, we do the same calculation for
394 differences in the rebound period (the period after the restrictions were relaxed) from the lockdown
395 period (Rebound – Lock) in 2020 and compare them with Rebound – Lock for the reference years
396 2016 – 2019 (**Figure 4d**). We observe a clear delay in the evolution of ammonia emissions in 2020
397 of -77 kt (**Figure 4c**), while only Scandinavian countries show positive changes. Hot-spots of
398 negative evolution were seen in central Europe, mainly in the triptych of Northern Italy, Switzerland
399 and Austria, for the reasons discussed in the previous paragraph. In Poland, the Ministry of Health
400 enforced self-isolation measures and restrictions on civic freedoms, including access to public spaces,
401 to contain the transmission of the disease. These measures significantly affected the daily lives of
402 Polish citizens (Szczepańska and Pietrzyka, 2021) and might be the reason for the decreased evolution
403 of ammonia emissions (**Figure 4c**). After the measures were relaxed, the evolution of the emissions
404 rebounded slightly with respect to the reference period (2016 – 2019) as shown in **Figure 4d**. The
405 changes in ammonia during the rebound period were concentrated in countries that were affected
406 most severely from the lockdown restrictions, namely Northern Italy, Switzerland, Austria and
407 Poland. The same has been reported for several other pollutant emissions (Davis et al., 2022; Jackson
408 et al., 2022).



409 3.4 Uncertainty of the posterior emissions

410 As described in section 2.3 in more detail, we considered 4° surroundings of each spatial
411 element of our inversion domain from which the CrIS observations were used in the inverse problem.
412 This means that 45 spatial elements in CrIS space were used, with six vertical levels each, for each
413 of the 26 temporal emission elements. To calculate the associated uncertainty of the posterior
414 estimates, we tested two sources of uncertainty: (i) how different surroundings for each spatial
415 element affect posterior emissions of ammonia and (ii) how the use of different prior emissions affects
416 posterior ammonia. We organized a series of sensitivity tests using surroundings covering 2°, 3° and
417 4° from each grid-cell. This selection is realistic as it was shown previously in Cao et al. (2020) for
418 the construction of prior emission error covariance matrix. For the second source of uncertainty, we
419 performed the same inversion using not only EC6G4 and VD priors, but also adding results using two
420 more datasets for ammonia (in total four), which have 10 times higher emissions, namely EGG and
421 NE (see section 2.3).

422 The calculated absolute uncertainties are depicted in **Figure 5a–c** together with the relative
423 uncertainty (**Figure 5d**) with respect to the posterior emissions of ammonia (posterior ammonia is
424 shown in **Figure 2c**). The first source of uncertainty (different surroundings) slightly affects the
425 resulting posterior emissions of ammonia (**Figure 5a**) causing an average relative uncertainty below
426 4% in the European emissions. The second source of uncertainty (use of different priors) causes much
427 larger bias as shown in **Figure 5b** (average relative uncertainty 35%). The reason for this is obviously
428 the large variation of the EGG (Bouwman et al., 1997; Giglio et al., 2013; Klimont et al., 2017) and
429 NE (Evangelidou et al., 2021) prior datasets that have total emissions in the first half of 2020 of 63.5
430 and 53.3 Tg, respectively, in contrast to only 6.2 and 5.7 Tg for EC6G4 and VD. Hence, the results
431 presented here are sensitive to the use of prior emission dataset. The modelled concentrations (that
432 replaces the hypothetical true column concentration in Eq. 1) is calculated by the SRMs and the prior
433 emission and, therefore, play a key role in the comparison of the CrIS value (v^{sat}) and retrieved value
434 (v^{ret}) (see Eq. 2). Also, the modelled concentrations stand as the argument of the natural logarithm
435 weighted by the averaging kernel in logarithmic space. The linearization of this operator as suggested
436 by Sitwell and Shephard (2021) may reduce the dependency on the prior emission term, however,
437 this is beyond the scope of this study. Overall, the propagated (absolute and relative) uncertainties of
438 the posterior emissions are shown in **Figure 5c** and **d** and are equal to 11% over Europe on average
439 (**Figure 5**). The latter shows that our calculations are robust on one hand, but dependent on the use
440 of a priori information on the other.



441 **4 Discussion**

442 **4.1 Rising ammonia concentrations during the European lockdowns**

443 One issue that has been overlooked is the concentrations of ammonia before, during and after
444 the 2020 lockdowns in Europe. Despite the delay in the emissions during the lockdown period in
445 2020, the measured atmospheric levels of ammonia recorded in CrIS showed an increase during the
446 lockdowns and declined after the restrictions were relaxed in almost all European countries (**Figure**
447 **3**). The latter was reported in several studies analysing ground-based measurements. For example,
448 Lovarelli et al. (2021) concluded that contrary to other air pollutants, ammonia was not reduced when
449 the COVID-19 restrictions were introduced in North Italy, as agricultural activity, which is the main
450 emissive source of this pollutant, was not interrupted. They further report that urban and rural
451 ammonia was the highest compared to previous years during the same months for which the strictest
452 lockdowns took place (i.e., spring 2020). Rennie et al. (2020) reported a slight decrease of ammonia
453 in the UK, while Xu et al. (2022) observed increased of ambient ammonia during the lockdowns in
454 China. Accordingly, Viatte et al. (2021) found enhanced ammonia during lockdown in Paris. Finally,
455 in a recent study, Kuttippurath et al. (2023) reported increases in ammonia during lockdowns almost
456 everywhere, with maxima in Western Europe, Eastern China, the Indian subcontinent and the Eastern
457 USA. Since atmospheric ammonia has been increasing globally due to various anthropogenic
458 activities, the European lockdowns in 2020 offer a unique opportunity to expose ammonia's sources
459 and address the importance of secondary PM_{2.5} formation.

460 **Figure 6a** depicts the modelled atmospheric lifetime of ammonia and its dependence from the
461 calculated loss-rates over Europe for the first half of 2020. Ammonia is a particularly interesting
462 substance due to its affinity to react with atmospheric acids producing secondary aerosols. In most
463 cases, it is depleted by sulfuric and nitric acids. In principle, the neutralisation of sulfuric acid is faster
464 and sulfuric acid more abundant in the atmosphere than nitric acid (Evangelidou et al., 2021), so that
465 ammonia is depleted directly (almost instantaneous in models, with almost 30 minutes timesteps).
466 Results from laboratory and field studies (Weber et al., 1999; Schobesberger et al., 2015) suggest that
467 ammonia actually promotes the nucleation of sulfuric acid in the atmosphere. This effect is not well
468 understood and results in rates of particle nucleation in the atmosphere that appear to be much faster
469 than expected based on the theory. After the reaction with sulfuric acid, free ammonia can further
470 react with nitric acid to form ammonium nitrate. However, in certain atmospheric conditions (e.g.,
471 high humidity, aqueous particles), the equilibrium vapor pressure of ammonia with nitric acid
472 increases shifting the reaction with nitric acid towards production of free ammonia (Seinfeld and
473 Pandis, 2000). However, production of ammonia is a rare event in continental Europe (see details in
474 Tichý et al., 2023).



475 During the lockdown period over Europe, transport and industrial activities mostly stopped,
476 and consequently the related emissions also decreased. This had an immediate effect on SO_2 and NO_x
477 (Guevara et al., 2021; Doumbia et al., 2021). Reductions of SO_2 and NO_x caused less production of
478 atmospheric sulfuric and nitric acids. The latter had a rapid twofold effect on the lifetime of ammonia:
479 (i) Less available atmospheric acids needed less ammonia for neutralisation towards sulfate (mainly)
480 and nitrate aerosols and therefore the loss-rates declined (**Figure 6a**) leading to accumulation of
481 ammonia in its free form; (ii) ammonia originates mainly from agriculture and livestock, and these
482 activities did not stop during the European lockdowns increasing the associated emissions (see **Figure**
483 **2**, though with a lower trend than previous years as discussed in section 3.3). The rising levels of
484 ammonia during the COVID-19 lockdowns in Europe have been confirmed by the CrIS observations
485 (**Figure 2** and **3**) and have been also reported elsewhere (Kuttippurath et al., 2023; Viatte et al., 2021;
486 Xu et al., 2022; Lovarelli et al., 2021).

487 **4.2 Disturbance in the secondary formation of PM_{2.5}**

488 The response of the restriction measures on PM_{2.5} mass concentrations suggests a
489 relationship that is more complex than expected and beyond road traffic intensity, at least for Europe.
490 It has been reported that there was no systematic decrease in PM_{2.5} concentrations during COVID-
491 19 lockdowns in USA (Archer et al., 2020; Bekbulat et al., 2021) or even in Chinese cities (Mo et al.,
492 2021), where primary sources are abundant and stringent lockdown measures decreased PM levels
493 (Zhang et al., 2023). In a recent study focusing on PM_{2.5} measurements over 30 urban and regional
494 background European sites, Putaud et al. (2023) showed that the implementation of the lockdown
495 measures resulted in minor increases in PM_{2.5} mass concentration in Europe of $+5\pm 33\%$. The latter
496 aligns well with several regional studies focusing on the impact of lockdowns to regional pollution
497 (Querol et al., 2021; Shi et al., 2021; Viatte et al., 2021; Thunis et al., 2021; Putaud et al., 2021).

498 **Figure 6b** demonstrates observed PM_{2.5} from the EMEP stations (78 sites) in comparison
499 with modelled PM_{2.5} concentrations, both averaged for all sites. In modelled PM_{2.5} mass
500 concentrations, we have separated primary and secondary PM_{2.5}, as secondary PM_{2.5} is modulated
501 by the chemical state of the atmosphere as defined by the abundance in acids and free ammonia. We
502 see that observed and modelled PM_{2.5} concentrations are in good agreement in the first half of 2020.
503 The good agreement between modelled and observed concentrations can be also confirmed for most
504 of the EMEP stations over Europe with high Pearson's coefficients, low RMSE's and low standard
505 deviations in the Taylor plot that is demonstrated in **Figure S 6**. Furthermore, while secondary PM_{2.5}
506 constitute around 20-30% of the total PM_{2.5} (Dat et al., 2024; Bressi et al., 2013; Li et al., 2023), this
507 proportion increased during the European lockdowns despite that reactions of ammonia to form
508 PM_{2.5} were decelerated (as seen by the declined loss in **Figure 6a**).



509 Leung et al. (2020) reported that the abatement of nitrate in China is buffered not only by
510 increased oxidant build-up, but also by sulfate to nitrate conversion and liberation of free ammonia
511 through sulfate concentration reduction, which favours nitrate formation. During COVID-19
512 restrictions in Europe, a significant decrease of NO_x (and SO_2) emissions occurred (Guevara et al.,
513 2021) also confirmed by Doumbia et al. (2021). Thunis et al. (2021) showed that the latter might have
514 increased the oxidative capacity of the atmosphere and, in turn, PM_{2.5} formation. This is the main
515 reason why PM_{2.5} concentrations were not decreased during the COVID-19 lockdowns in many
516 European cities (Varotsos et al., 2021; Shi et al., 2021), while the same has been reported elsewhere
517 (Huang et al., 2021; Le et al., 2020; Zhang et al., 2022).

518 PM_{2.5} increased at areas less affected by primary emissions during the 2020 lockdowns or at
519 areas where the oxidative atmosphere favours secondary aerosol formation. For instance, reductions
520 in PM_{2.5} were observed to be less pronounced than those in nitrogen dioxide in several regions (Patel
521 et al., 2020; Shi and Brasseur, 2020), while PM_{2.5} even increased in others (Wang et al., 2020; Li et
522 al., 2020). Li et al. (2020) indicated that while primary emissions dropped by 15–61% in China, daily
523 average PM_{2.5} concentrations were still very high (15–79 $\mu\text{g m}^{-3}$) showing that background and
524 residual pollutants were important. In a similar manner, an extreme PM_{2.5} pollution event during the
525 Chinese lockdown in Nanning that cause public concern was due to secondary aerosol formation (Mo
526 et al., 2021).

527 Here we aim at interpreting the mechanism below this disturbance in PM_{2.5} formation. As
528 explained in Seinfeld and Pandis (2000), the neutralisation of atmospheric acids by ammonia in the
529 atmosphere occurs directly to ammonium sulfate ($(NH_4)_2SO_{4(s)}$) in the gas phase or to ammonium
530 ($NH_4^+(aq)$) and sulfate ($SO_4^{2-}(aq)$) with an intermediate product (ammonium, $NH_4^+(aq)$, and bisulfate,
531 $HSO_4^-(aq)$) in the aqueous phase. Sulfate ($SO_4^{2-}(s)$) can be also produced in the gas phase from sulfur
532 dioxide ($SO_{2(g)}$) with hydroxyl radical (OH) as the oxidant. Note that hydroxyl radical is formed in
533 the atmosphere when ultraviolet light (UV) from the sun strikes ozone in the presence of water
534 vapour, hence it is linked to humidity (**Figure S 7**). Sulfate production can also occur in the aqueous
535 phase (Hoyle et al., 2016) through sulfur dioxide ($SO_{2(aq)}$) oxidation with ozone ($O_{3(aq)}$) or
536 hydrogen peroxide ($H_2O_{2(aq)}$). In both phases, higher humidity favours sulfate formation (**Figure S**
537 **7**). Ammonia also reacts with nitric acid ($HNO_{3(g)}$) to form nitrate ($NO_3^-(s)$) in an equilibrium
538 reaction that is rare. In that case, as SO_2 is strongly decreased due to the restrictions (Doumbia et al.,
539 2021) and more free ammonia accumulates (see previous section), these higher gaseous ammonia
540 levels shift the equilibrium reaction towards a larger conversion of gaseous nitric acid into particulate
541 nitrate. This mechanism has been highlighted in China as an unintended consequence of the of NO_x
542 and SO_2 regulation on the PM_{2.5} levels (Lachatre et al., 2019). Wang et al. (2022) recently reported



543 that NH_3 - H_2SO_4 - HNO_3 form particles synergistically, at rates orders of magnitude faster than those
544 from any two of the three components and that the reaction rates are controlled by the availability of
545 NH_3 . In addition to this mechanism, as the fraction of total inorganic nitrate, as particulate $NO_3^-_{(s)}$
546 instead of gaseous $HNO_3_{(g)}$, increases, as emissions of NO_x and SO_2 decrease, while NH_3 emissions
547 remain high, a small increase in the particulate fraction greatly slows down deposition of total
548 inorganic $NO_3^-_{(s)}$ and hence drives the particulate $NO_3^-_{(s)}$ increase (Zhai et al., 2021). Thus, although
549 NO_x emissions decreased during COVID-19 lockdowns in Europe, secondary PM_{2.5} stayed
550 unchanged, because NO_x emissions reduction drives faster oxidation of NO_x and slower deposition
551 of total inorganic $NO_3^-_{(s)}$.

552 5 Conclusion

553 We have examined the impact of lockdown measures in Europe due to COVID-19 on the
554 atmospheric levels and emissions of ammonia using high-resolution satellite observations combined
555 with a dispersion model and an inverse modelling algorithm. We find that ammonia emissions in
556 2020 declined by -9.8% as compared to the same period in previous years (2016–2019). However,
557 this decrease appears to be insensitive to the meteorological conditions, as ammonia emissions in the
558 2020 lockdowns dropped under the variance of emissions calculated for the reference period (2016–
559 2019). Ammonia emissions increase in spring and late summer in Europe because of agriculture and
560 temperature dependent volatilization. Though during the lockdowns of 2020, a clear delay in the
561 evolution of ammonia emissions of -77 kt was found, mostly in the central European countries, which
562 suffered by the stringent restrictions. The evolution of ammonia emissions slightly rebounded after
563 the restrictions were relaxed.

564 During the COVID-19 lockdowns of 2020 the atmospheric levels of ammonia were drastically
565 increased, as confirmed by ground-based and satellite observations over Europe. The reason for this
566 is twofold; first, the European lockdown measures decreased atmospheric emissions and levels of
567 SO_2 and NO_x and their acidic products (H_2SO_4 and HNO_3) slowing down binding and chemical
568 removal of ammonia (lifetimes increased), and thus accumulating free ammonia; second, agricultural
569 activity never ceased constantly increasing ammonia emissions during the lockdowns, though at a
570 lower rate.

571 Surprisingly, despite all the travel, working and social restrictions that the European
572 governments took to combat the outbreak of COVID-19, ambient pollution levels did not increase as
573 expected. PM_{2.5} levels were modulated by the chemical state of the atmosphere through secondary
574 aerosol formation. Secondary PM_{2.5} increased during the European lockdowns despite that the



575 precursors of H_2SO_4 and HNO_3 declined. More sulfate was produced from SO_2 and OH (gas phase)
576 or O_3 (aqueous phase), while both atmospheric reactions were favoured by higher water vapour
577 content (humidity) during the lockdown period. The accumulated ammonia neutralised the more
578 abundant H_2SO_4 first producing sulfate. Then, as SO_2 decreased during the European lockdowns and
579 more free ammonia accumulated, the high excess gaseous ammonia neutralised HNO_3 shifting the
580 equilibrium reaction towards conversion to particulate nitrate causing unintended increase in the
581 $PM_{2.5}$ levels. While NO_x emissions declined during the European lockdowns by -33%, this reduction
582 drives faster oxidation of NO_x and slower deposition of total inorganic nitrate causing high secondary
583 $PM_{2.5}$ levels.

584 The present study gives a comprehensive analysis of the atmospheric system $NH_3 - H_2SO_4 -$
585 HNO_3 . It also proves the complicated relationship of secondary $PM_{2.5}$ formation with the abundant
586 atmospheric gases. The general drop of emissions during the first consistent lockdowns of 2020 is
587 Europe offers a unique opportunity to study their atmospheric chemistry under extreme conditions of
588 fast pollutant emission drop equivalent to “The Clean Air Action” of the Chinese government.

589

590 **Data availability.** All data from this study are available for download from
591 <https://datadryad.org/stash/share/Wgbc9UiXwtMH44366myWh2bt7MQc92JKhJBz7UwOlgY>
592 (reserved doi: 10.5061/dryad.12jm63z1q). The EMEP measurements of ammonia can be downloaded
593 from <https://ebas.nilu.no>. The remote sensing data for ammonia can be retrieved from
594 https://hpfx.collab.science.gc.ca/~mas001/satellite_ext/cris/snpp/nh3/v1_6_4/ or upon request to Dr.
595 M. W. Shephard. FLEXPART version 10.4 model can be downloaded from
596 <https://www.flexpart.eu/downloads>.

597

598 **Supplement.** The supplement related to this article is available online at.

599

600 **Author contributions.** NE led the overall study, analysed the results and wrote the paper. OT
601 developed the inverse modelling algorithm and performed the inversions. MSO processed CrIS
602 ammonia on a grid. SE developed FLEXPART version 10.4 model to account for the loss of ammonia
603 from the chemistry transport model LMDz-OR-INCA. YB and DH set up and ran the chemistry
604 transport model LMDz-OR-INCA. All authors contributed to the final version of the manuscript.

605

606 **Competing interests.** The authors declare no competing interests.

607



608 **Financial support.** The work was supported by the COMBAT (Quantification of Global Ammonia
609 Sources constrained by a Bayesian Inversion Technique) project funded by ROMFORSK – Program
610 for romforskning of the Research Council of Norway (Project ID: 275407, website:
611 <https://prosjektbanken.forskingsradet.no/project/FORISS/275407?Kilde=FORISS&distribution=Ar&chart=bar&calcType=funding&Sprak=no&sortBy=date&sortOrder=desc&resultCount=30&offset=0&ProgAkt.3=ROMFORSK-Program+for+romforskning>). Dr. Ondřej Tichý was supported by the
614 Czech Science Foundation, grant no. GA20-27939S.

615

616 **References**

- 617 Abbatt, J. P. D., Benz, S., Cziczo, D. J., Kanji, Z., Lohmann, U., and Mohler, O.: Solid Ammonium
618 Sulfate Aerosols as Ice Nuclei: A Pathway for Cirrus Cloud Formation, *Science* (80-.), 313, 1770–
619 1773, 2006.
- 620 Acharya, P., Barik, G., Gayen, B. K., Bar, S., Maiti, A., Sarkar, A., Ghosh, S., De, S. K., and
621 Sreekish, S.: Revisiting the levels of Aerosol Optical Depth in south-southeast Asia, Europe and
622 USA amid the COVID-19 pandemic using satellite observations, *Environ. Res.*, 193, 110514,
623 <https://doi.org/10.1016/j.envres.2020.110514>, 2021.
- 624 Anderson, N., Strader, R., and Davidson, C.: Airborne reduced nitrogen: Ammonia emissions from
625 agriculture and other sources, *Environ. Int.*, 29, 277–286, [https://doi.org/10.1016/S0160-](https://doi.org/10.1016/S0160-4120(02)00186-1)
626 [4120\(02\)00186-1](https://doi.org/10.1016/S0160-4120(02)00186-1), 2003.
- 627 Archer, C. L., Cervone, G., Golbazi, M., Al Fasel, N., and Hultquist, C.: Changes in air quality and
628 human mobility in the USA during the COVID-19 pandemic, *Bull. Atmos. Sci. Technol.*, 1, 491–
629 514, <https://doi.org/10.1007/s42865-020-00019-0>, 2020.
- 630 Baekgaard, M., Christensen, J., Madsen, J. K., and Mikkelsen, K. S.: Rallying around the flag in
631 times of COVID-19: Societal lockdown and trust in democratic institutions, *J. Behav. Public Adm.*,
632 3, 1–12, <https://doi.org/10.30636/jbpa.32.172>, 2020.
- 633 Bauwens, M., Compernelle, S., Stavrakou, T., Müller, J. F., van Gent, J., Eskes, H., Levelt, P. F.,
634 van der A, R., Veefkind, J. P., Vlietinck, J., Yu, H., and Zehner, C.: Impact of Coronavirus
635 Outbreak on NO₂ Pollution Assessed Using TROPOMI and OMI Observations, *Geophys. Res.*
636 *Lett.*, 47, 1–9, <https://doi.org/10.1029/2020GL087978>, 2020.
- 637 Bekbulat, B., Apte, J. S., Millet, D. B., Robinson, A. L., Wells, K. C., Presto, A. A., and Marshall,
638 J. D.: Changes in criteria air pollution levels in the US before, during, and after Covid-19 stay-at-
639 home orders: Evidence from regulatory monitors, *Sci. Total Environ.*, 769, 144693,
640 <https://doi.org/10.1016/j.scitotenv.2020.144693>, 2021.
- 641 Bellouin, N., Rae, J., Jones, A., Johnson, C., Haywood, J., and Boucher, O.: Aerosol forcing in the
642 Climate Model Intercomparison Project (CMIP5) simulations by HadGEM2-ES and the role of



- 643 ammonium nitrate, *J. Geophys. Res. Atmos.*, 116, 1–25, <https://doi.org/10.1029/2011JD016074>,
644 2011.
- 645 Bendz, B. and Aaberge, L.: COVID-19 spread in the UK: the end of the beginning?, *Lancet*, 396,
646 587–590, [https://doi.org/https://doi.org/10.1016/S0140-6736\(20\)31689-5](https://doi.org/https://doi.org/10.1016/S0140-6736(20)31689-5) www.thelancet.com,
647 2020.
- 648 Bouwman, A. F., Lee, D. S., Asman, W. A. H., Dentener, F. J., Van Der Hoek, K. W., and Olivier,
649 J. G. J.: A global high-resolution emission inventory for ammonia, *Global Biogeochem. Cycles*, 11,
650 561–587, <https://doi.org/10.1029/97GB02266>, 1997.
- 651 Bressi, M., Sciare, J., Ghersi, V., Bonnaire, N., Nicolas, J. B., Petit, J. E., Moukhtar, S., Rosso, A.,
652 Mihalopoulos, N., and Féron, A.: A one-year comprehensive chemical characterisation of fine
653 aerosol (PM_{2.5}) at urban, suburban and rural background sites in the region of Paris (France),
654 *Atmos. Chem. Phys.*, 13, 7825–7844, <https://doi.org/10.5194/acp-13-7825-2013>, 2013.
- 655 Camargo, J. A. and Alonso, Á.: Ecological and toxicological effects of inorganic nitrogen pollution
656 in aquatic ecosystems: A global assessment, *Environ. Int.*, 32, 831–849,
657 <https://doi.org/10.1016/j.envint.2006.05.002>, 2006.
- 658 Cao, H., Henze, D. K., Shephard, M. W., Dammers, E., Cady-Pereira, K., Alvarado, M., Lonsdale,
659 C., Luo, G., Yu, F., Zhu, L., Danielson, C. G., and Edgerton, E. S.: Inverse modeling of NH₃
660 sources using CrIS remote sensing measurements, *Environ. Res. Lett.*, 15, 104082,
661 <https://doi.org/10.1088/1748-9326/abb5cc>, 2020.
- 662 Cassiani, M., Stohl, A., and Brioude, J.: Lagrangian Stochastic Modelling of Dispersion in the
663 Convective Boundary Layer with Skewed Turbulence Conditions and a Vertical Density Gradient:
664 Formulation and Implementation in the FLEXPART Model, *Boundary-Layer Meteorol.*, 154, 367–
665 390, <https://doi.org/10.1007/s10546-014-9976-5>, 2014.
- 666 Chakraborty, I. and Maity, P.: COVID-19 outbreak: Migration, effects on society, global
667 environment and prevention, *Sci. Total Environ.*, 728, 138882,
668 <https://doi.org/10.1016/j.scitotenv.2020.138882>, 2020.
- 669 Chen, S., Perathoner, S., Ampelli, C., and Centi, G.: Chapter 2 - Electrochemical Dinitrogen
670 Activation: To Find a Sustainable Way to Produce Ammonia, in: *Horizons in Sustainable Industrial*
671 *Chemistry and Catalysis*, vol. 178, edited by: Albonetti, S., Perathoner, S., and Quadrelli, E. A. B.
672 T.-S. in S. S. and C., Elsevier, 31–46, [https://doi.org/https://doi.org/10.1016/B978-0-444-64127-](https://doi.org/https://doi.org/10.1016/B978-0-444-64127-4.00002-1)
673 [4.00002-1](https://doi.org/https://doi.org/10.1016/B978-0-444-64127-4.00002-1), 2019.
- 674 Cohen, A. J., Brauer, M., Burnett, R., Anderson, H. R., Frostad, J., Estep, K., Balakrishnan, K.,
675 Brunekreef, B., Dandona, L., Dandona, R., Feigin, V., Freedman, G., Hubbell, B., Jobling, A., Kan,
676 H., Knibbs, L., Liu, Y., Martin, R., Morawska, L., Pope, C. A., Shin, H., Straif, K., Shaddick, G.,
677 Thomas, M., van Dingenen, R., van Donkelaar, A., Vos, T., Murray, C. J. L., and Forouzanfar, M.



678 H.: Estimates and 25-year trends of the global burden of disease attributable to ambient air
679 pollution: an analysis of data from the Global Burden of Diseases Study 2015, *Lancet*, 389, 1907–
680 1918, [https://doi.org/10.1016/S0140-6736\(17\)30505-6](https://doi.org/10.1016/S0140-6736(17)30505-6), 2017.

681 Croft, B., Pierce, J. R., and Martin, R. V.: Interpreting aerosol lifetimes using the GEOS-Chem
682 model and constraints from radionuclide measurements, *Atmos. Chem. Phys.*, 14, 4313–4325,
683 <https://doi.org/10.5194/acp-14-4313-2014>, 2014.

684 Van Damme, M., Clarisse, L., Whitburn, S., Hadji-Lazaro, J., Hurtmans, D., Clerbaux, C., and
685 Coheur, P. F.: Industrial and agricultural ammonia point sources exposed, *Nature*, 564, 99–103,
686 <https://doi.org/10.1038/s41586-018-0747-1>, 2018.

687 Van Damme, M., Clarisse, L., Franco, B., Sutton, M. A., Erisman, J. W., Wichink Kruit, R., Van
688 Zanten, M., Whitburn, S., Hadji-Lazaro, J., Hurtmans, D., Clerbaux, C., and Coheur, P. F. ois:
689 Global, regional and national trends of atmospheric ammonia derived from a decadal (2008–2018)
690 satellite record, *Environ. Res. Lett.*, 16, <https://doi.org/10.1088/1748-9326/abd5e0>, 2021.

691 Van Damme, M., Clarisse, L., Stavrou, T., Wichink Kruit, R., Sellekaerts, L., Viatte, C.,
692 Clerbaux, C., and Coheur, P. F.: On the weekly cycle of atmospheric ammonia over European
693 agricultural hotspots, *Sci. Rep.*, 12, 1–9, <https://doi.org/10.1038/s41598-022-15836-w>, 2022.

694 Dammers, E., Shephard, M. W., Palm, M., Cady-pereira, K., Capps, S., Lutsch, E., Strong, K.,
695 Hannigan, J. W., Ortega, I., Toon, G. C., Stremme, W., and Grutter, M.: Validation of the CrIS fast
696 physical NH₃ retrieval with ground-based FTIR, *Atmos. Meas. Tech.*, 87, 2645–2667, 2017.

697 Dat, N. Q., Ly, B. T., Nghiem, T. D., Nguyen, T. T. H., Sekiguchi, K., Huyen, T. T., Vinh, T. H.,
698 and Tien, L. Q.: Influence of Secondary Inorganic Aerosol on the Concentrations of PM_{2.5} and
699 PM_{0.1} during Air Pollution Episodes in Hanoi, Vietnam, *Aerosol Air Qual. Res.*, 24,
700 <https://doi.org/10.4209/aaqr.220446>, 2024.

701 Davis, S. J., Liu, Z., Deng, Z., Zhu, B., Ke, P., Sun, T., Guo, R., Hong, C., Zheng, B., Wang, Y.,
702 Boucher, O., Gentine, P., and Ciaia, P.: Emissions rebound from the COVID-19 pandemic, *Nat.*
703 *Clim. Chang.*, 12, 410–417, <https://doi.org/10.1038/s41558-022-01351-3>, 2022.

704 Diffenbaugh, N. S., Field, C. B., Appel, E. A., Azevedo, I. L., Baldocchi, D. D., Burke, M., Burney,
705 J. A., Ciaia, P., Davis, S. J., Fiore, A. M., Fletcher, S. M., Hertel, T. W., Horton, D. E., Hsiang, S.
706 M., Jackson, R. B., Jin, X., Levi, M., Lobell, D. B., McKinley, G. A., Moore, F. C., Montgomery,
707 A., Nadeau, K. C., Pataki, D. E., Randerson, J. T., Reichstein, M., Schnell, J. L., Seneviratne, S. I.,
708 Singh, D., Steiner, A. L., and Wong-Parodi, G.: The COVID-19 lockdowns: a window into the
709 Earth System, *Nat. Rev. Earth Environ.*, 1–12, <https://doi.org/10.1038/s43017-020-0079-1>, 2020.

710 Doumbia, T., Granier, C., Elguindi, N., Bouarar, I., Darras, S., Brasseur, G., Gaubert, B., Liu, Y.,
711 Shi, X., Stavrou, T., Tilmes, S., Lacey, F., Deroubaix, A., and Wang, T.: Changes in global air
712 pollutant emissions during the COVID-19 pandemic: A dataset for atmospheric modeling, *Earth*



- 713 Syst. Sci. Data, 13, 4191–4206, <https://doi.org/10.5194/essd-13-4191-2021>, 2021.
- 714 Dutheil, F., Baker, J. S., and Navel, V.: COVID-19 as a factor influencing air pollution?, Environ.
715 Pollut., 263, 2019–2021, <https://doi.org/10.1016/j.envpol.2020.114466>, 2020.
- 716 Emanuel, K. A.: A Scheme for Representing Cumulus Convection in Large-Scale Models, J.
717 Atmos. Sci., 48, 2313–2329, [https://doi.org/10.1175/1520-0469\(1991\)048<2313:ASFRCC>2.0.CO;2](https://doi.org/10.1175/1520-0469(1991)048<2313:ASFRCC>2.0.CO;2), 1991.
- 719 Erisman, J. W., Bleeker, A., Galloway, J., and Sutton, M. S.: Reduced nitrogen in ecology and the
720 environment, Environ. Pollut., 150, 140–149, <https://doi.org/10.1016/j.envpol.2007.06.033>, 2007.
- 721 Erisman, J. W., Sutton, M. a., Galloway, J., Klimont, Z., and Winiwarter, W.: How a century of
722 ammonia synthesis changed the world, Nat. Geosci., 1, 636–639, <https://doi.org/10.1038/ngeo325>,
723 2008.
- 724 Evangeliou, N., Platt, S., Eckhardt, S., Lund Myhre, C., Laj, P., Alados-Arboledas, L., Backman, J.,
725 Brem, B., Fiebig, M., Flentje, H., Marinoni, A., Pandolfi, M., Yus-Diez, J., Prats, N., Putaud, J.,
726 Sellegri, K., Sorribas, M., Eleftheriadis, K., Vratolis, S., Wiedensohler, A., and Stohl, A.: Changes
727 in black carbon emissions over Europe due to COVID-19 lockdowns, Atmos. Chem. Phys., 1–33,
728 <https://doi.org/10.5194/acp-2020-1005>, 2020.
- 729 Evangeliou, N., Balkanski, Y., Eckhardt, S., Cozic, A., Van Damme, M., Coheur, P.-F., Clarisse,
730 L., Shephard, M., Cady-Pereira, K., and Hauglustaine, D.: 10-Year Satellite-Constrained Fluxes of
731 Ammonia Improve Performance of Chemistry Transport Models, Atmos. Chem. Phys., 21, 4431–
732 4451, <https://doi.org/10.5194/acp-21-4431-2021>, 2021.
- 733 Folberth, G. A., Hauglustaine, D. A., Lathière, J., and Brocheton, F.: Interactive chemistry in the
734 Laboratoire de Météorologie Dynamique general circulation model: model description and impact
735 analysis of biogenic hydrocarbons on tropospheric chemistry, Atmos. Chem. Phys., 6, 2273–2319,
736 <https://doi.org/10.5194/acp-6-2273-2006>, 2006.
- 737 Forster, C., Stohl, A., and Seibert, P.: Parameterization of convective transport in a Lagrangian
738 particle dispersion model and its evaluation, J. Appl. Meteorol. Climatol., 46, 403–422,
739 <https://doi.org/10.1175/JAM2470.1>, 2007.
- 740 Fowler, D., Muller, J. B. A., Smith, R. I., Dragosits, U., Skiba, U., Sutton, M. A., and
741 Brimblecombe, P.: A CHRONOLOGY OF NITROGEN DEPOSITION IN THE UK, Water, Air,
742 Soil Pollut. Focus, 4, 9–23, 2004.
- 743 Ge, X., Schaap, M., Kranenburg, R., Segers, A., Jan Reinds, G., Kros, H., and De Vries, W.:
744 Modeling atmospheric ammonia using agricultural emissions with improved spatial variability and
745 temporal dynamics, Atmos. Chem. Phys., 20, 16055–16087, [https://doi.org/10.5194/acp-20-16055-](https://doi.org/10.5194/acp-20-16055-2020)
746 2020, 2020.
- 747 Giani, P., Castruccio, S., Anav, A., Howard, D., Hu, W., and Crippa, P.: Short-term and long-term



748 health impacts of air pollution reductions from COVID-19 lockdowns in China and Europe: a
749 modelling study, *Lancet Planet. Heal.*, 4, e474–e482, [https://doi.org/10.1016/S2542-](https://doi.org/10.1016/S2542-5196(20)30224-2)
750 5196(20)30224-2, 2020.

751 Giglio, L., Randerson, J. T., and van der Werf, G. R.: Analysis of daily, monthly, and annual burned
752 area using the fourth-generation global fire emissions database (GFED4), *J. Geophys. Res.*
753 *Biogeosciences*, 118, 317–328, <https://doi.org/10.1002/jgrg.20042>, 2013, 2013.

754 Gordon, D. V., Grafton, R. Q., and Steinshamn, S. I.: Cross-country effects and policy responses to
755 COVID-19 in 2020: The Nordic countries, *Econ. Anal. Policy*, 71, 198–210,
756 <https://doi.org/10.1016/j.eap.2021.04.015>, 2021.

757 Gu, B., Sutton, M. A., Chang, S. X., Ge, Y., and Chang, J.: Agricultural ammonia emissions
758 contribute to China’s urban air pollution, *Front. Ecol. Environ.*, 12, 265–266,
759 <https://doi.org/10.1890/14.WB.007>, 2014.

760 Guevara, M., Jorba, O., Soret, A., Petetin, H., Bowdalo, D., Serradell, K., Tena, C., Van Der Gon,
761 H. D., Kuenen, J., Peuch, V. H., and Pérez García-Pando, C.: Time-resolved emission reductions for
762 atmospheric chemistry modelling in Europe during the COVID-19 lockdowns, *Atmos. Chem.*
763 *Phys.*, 21, 773–797, <https://doi.org/10.5194/acp-21-773-2021>, 2021.

764 Hauglustaine, D. A., Hourdin, F., Jourdain, L., Filiberti, M.-A., Walters, S., Lamarque, J.-F., and
765 Holland, E. A.: Interactive chemistry in the Laboratoire de Meteorologie Dynamique general
766 circulation model: Description and background tropospheric chemistry evaluation, *J. Geophys.*
767 *Res.*, 109, <https://doi.org/10.1029/2003JD003957>, 2004.

768 Hauglustaine, D. A., Balkanski, Y., and Schulz, M.: A global model simulation of present and
769 future nitrate aerosols and their direct radiative forcing of climate, *Atmos. Chem. Phys.*, 14, 11031–
770 11063, <https://doi.org/10.5194/acp-14-11031-2014>, 2014.

771 Heald, C. L., Collett, J. L., Lee, T., Benedict, K. B., Schwandner, F. M., Li, Y., Clarisse, L.,
772 Hurtmans, D. R., Van Damme, M., Clerbaux, C., Coheur, P. F., Philip, S., Martin, R. V., and Pye,
773 H. O. T.: Atmospheric ammonia and particulate inorganic nitrogen over the United States, *Atmos.*
774 *Chem. Phys.*, 12, 10295–10312, <https://doi.org/10.5194/acp-12-10295-2012>, 2012.

775 Henze, D. K., Shindell, D. T., Akhtar, F., Spurr, R. J. D., Pinder, R. W., Loughlin, D., Kopacz, M.,
776 Singh, K., and Shim, C.: Spatially Refined Aerosol Direct Radiative Forcing Efficiencies, *Environ.*
777 *Sci. Technol.*, 46, 9511–9518, <https://doi.org/10.1021/es301993s>, 2012.

778 Hersbach, H., Bell, B., Berrisford, P., Hirahara, S., Horányi, A., Muñoz-Sabater, J., Nicolas, J.,
779 Peubey, C., Radu, R., Schepers, D., Simmons, A., Soci, C., Abdalla, S., Abellan, X., Balsamo, G.,
780 Bechtold, P., Biavati, G., Bidlot, J., Bonavita, M., De Chiara, G., Dahlgren, P., Dee, D.,
781 Diamantakis, M., Dragani, R., Flemming, J., Forbes, R., Fuentes, M., Geer, A., Haimberger, L.,
782 Healy, S., Hogan, R. J., Hólm, E., Janisková, M., Keeley, S., Laloyaux, P., Lopez, P., Lupu, C.,



- 783 Radnoti, G., de Rosnay, P., Rozum, I., Vamborg, F., Villaume, S., and Thépaut, J. N.: The ERA5
784 global reanalysis, *Q. J. R. Meteorol. Soc.*, 146, 1999–2049, <https://doi.org/10.1002/qj.3803>, 2020.
- 785 Hourdin, F. and Armengaud, A.: The Use of Finite-Volume Methods for Atmospheric Advection of
786 Trace Species. Part I: Test of Various Formulations in a General Circulation Model, *Mon. Weather*
787 *Rev.*, 127, 822–837, [https://doi.org/10.1175/1520-0493\(1999\)127<0822:TUOFVM>2.0.CO;2](https://doi.org/10.1175/1520-0493(1999)127<0822:TUOFVM>2.0.CO;2),
788 1999.
- 789 Hourdin, F., Musat, I., Bony, S., Braconnot, P., Codron, F., Dufresne, J. L., Fairhead, L., Filiberti,
790 M. A., Friedlingstein, P., Grandpeix, J. Y., Krinner, G., LeVan, P., Li, Z. X., and Lott, F.: The
791 LMDZ4 general circulation model: Climate performance and sensitivity to parametrized physics
792 with emphasis on tropical convection, *Clim. Dyn.*, 27, 787–813, [https://doi.org/10.1007/s00382-](https://doi.org/10.1007/s00382-006-0158-0)
793 [006-0158-0](https://doi.org/10.1007/s00382-006-0158-0), 2006.
- 794 Hoyle, C. R., Fuchs, C., Jarvinen, E., Saathoff, H., Dias, A., El Haddad, I., Gysel, M., Coburn, S.
795 C., Trostl, J., Hansel, A., Bianchi, F., Breitenlechner, M., Corbin, J. C., Craven, J., Donahue, N. M.,
796 Duplissy, J., Ehrhart, S., Frege, C., Gordon, H., Hoppel, N., Heinritzi, M., Kristensen, T. B.,
797 Molteni, U., Nichman, L., Pinterich, T., Prevôt, A. S. H., Simon, M., Slowik, J. G., Steiner, G.,
798 Tome, A., Vogel, A. L., Volkamer, R., Wagner, A. C., Wagner, R., Wexler, A. S., Williamson, C.,
799 Winkler, P. M., Yan, C., Amorim, A., Dommen, J., Curtius, J., Gallagher, M. W., Flagan, R. C.,
800 Hansel, A., Kirkby, J., Kulmala, M., Mohler, O., Stratmann, F., Worsnop, D. R., and Baltensperger,
801 U.: Aqueous phase oxidation of sulphur dioxide by ozone in cloud droplets, *Atmos. Chem. Phys.*,
802 16, 1693–1712, <https://doi.org/10.5194/acp-16-1693-2016>, 2016.
- 803 Huang, X., Ding, A., Gao, J., Zheng, B., Zhou, D., Qi, X., Tang, R., Wang, J., Ren, C., Nie, W.,
804 Chi, X., Xu, Z., Chen, L., Li, Y., Che, F., Pang, N., Wang, H., Tong, D., Qin, W., Cheng, W., Liu,
805 W., Fu, Q., Liu, B., Chai, F., Davis, S. J., Zhang, Q., and He, K.: Enhanced secondary pollution
806 offset reduction of primary emissions during COVID-19 lockdown in China, *Natl. Sci. Rev.*, 8,
807 <https://doi.org/10.1093/nsr/nwaa137>, 2021.
- 808 Jackson, R. B., Friedlingstein, P., Quéré, C. Le, Abernethy, S., Andrew, R. M., Canadell, J. G.,
809 Ciais, P., Davis, S. J., Deng, Z., Liu, Z., Korsbakken, J. I., and Peters, G. P.: Global fossil carbon
810 emissions rebound near pre-COVID-19 levels, *Environ. Res. Lett.*, 17,
811 <https://doi.org/https://doi.org/10.1088/1748-9326/ac55b6>, 2022.
- 812 Kean, A. J., Littlejohn, D., Ban-Weiss, G. A., Harley, R. A., Kirchstetter, T. W., and Lunden, M.
813 M.: Trends in on-road vehicle emissions of ammonia, *Atmos. Environ.*, 43, 1565–1570,
814 <https://doi.org/10.1016/j.atmosenv.2008.09.085>, 2009.
- 815 Kharol, S. K., Shephard, M. W., McLinden, C. A., Zhang, L., Sioris, C. E., O'Brien, J. M., Vet, R.,
816 Cady-Pereira, K. E., Hare, E., Siemons, J., and Krotkov, N. A.: Dry Deposition of Reactive
817 Nitrogen From Satellite Observations of Ammonia and Nitrogen Dioxide Over North America,



- 818 Geophys. Res. Lett., 45, 1157–1166, <https://doi.org/10.1002/2017GL075832>, 2018.
- 819 Klimont, Z.: personal communication, 2022.
- 820 Klimont, Z., Kupiainen, K., Heyes, C., Purohit, P., Cofala, J., Rafaj, P., Borken-Kleefeld, J., and
821 Schöpp, W.: Global anthropogenic emissions of particulate matter including black carbon, Atmos.
822 Chem. Phys., 17, 8681–8723, <https://doi.org/10.5194/acp-17-508681-2017>, 2017.
- 823 Krinner, G., Viovy, N., de Noblet-Ducoudré, N., Ogée, J., Polcher, J., Friedlingstein, P., Ciais, P.,
824 Sitch, S., and Prentice, I. C.: A dynamic global vegetation model for studies of the coupled
825 atmosphere-biosphere system, Global Biogeochem. Cycles, 19, GB1015,
826 <https://doi.org/10.1029/2003GB002199>, 2005.
- 827 Kristiansen, N. I., Stohl, A., Olivíe, D. J. L., Croft, B., Søvdé, O. A., Klein, H., Christoudias, T.,
828 Kunkel, D., Leadbetter, S. J., Lee, Y. H., Zhang, K., Tsigaridis, K., Bergman, T., Evangeliou, N.,
829 Wang, H., Ma, P. L., Easter, R. C., Rasch, P. J., Liu, X., Pitari, G., Di Genova, G., Zhao, S. Y.,
830 Balkanski, Y., Bauer, S. E., Faluvegi, G. S., Kokkola, H., Martin, R. V., Pierce, J. R., Schulz, M.,
831 Shindell, D., Tost, H., and Zhang, H.: Evaluation of observed and modelled aerosol lifetimes using
832 radioactive tracers of opportunity and an ensemble of 19 global models, 3525–3561 pp.,
833 <https://doi.org/10.5194/acp-16-3525-2016>, 2016.
- 834 Krupa, S. V.: Effects of atmospheric ammonia (NH₃) on terrestrial vegetation: A review, Environ.
835 Pollut., 124, 179–221, [https://doi.org/10.1016/S0269-7491\(02\)00434-7](https://doi.org/10.1016/S0269-7491(02)00434-7), 2003.
- 836 Kuhn, T.: The revision of the German Fertiliser Ordinance in 2017, Agric. Resour. Econ., 2, 1–22,
837 2017.
- 838 Kuttippurath, J., Patel, V. K., Kashyap, R., Singh, A., and Clerbaux, C.: Anomalous increase in
839 global atmospheric ammonia during COVID-19 lockdown: Need for policies to curb agricultural
840 emissions, J. Clean. Prod., 434, 140424, <https://doi.org/10.1016/j.jclepro.2023.140424>, 2023.
- 841 Lachatre, M., Fortems-Cheiney, A., Foret, G., Siour, G., Dufour, G., Clarisse, L., Clerbaux, C.,
842 Coheur, P. F., Van Damme, M., and Beekmann, M.: The unintended consequence of SO₂ and NO₂
843 regulations over China: Increase of ammonia levels and impact on PM_{2.5} concentrations, Atmos.
844 Chem. Phys., 19, 6701–6716, <https://doi.org/10.5194/acp-19-6701-2019>, 2019.
- 845 Le, T., Wang, Y., Liu, L., Yang, J., Yung, Y. L., Li, G., and Seinfeld, J. H.: Unexpected air
846 pollution with marked emission reductions during the COVID-19 outbreak in China, Science (80-
847), eabb7431, <https://doi.org/10.1126/science.abb7431>, 2020.
- 848 Lelieveld, J., Evans, J. S., Fnais, M., Giannadaki, D., and Pozzer, A.: The contribution of outdoor
849 air pollution sources to premature mortality on a global scale., Nature, 525, 367–71,
850 <https://doi.org/10.1038/nature15371>, 2015.
- 851 Leung, D. M., Shi, H., Zhao, B., Wang, J., Ding, E. M., Gu, Y., Zheng, H., Chen, G., Liou, K. N.,
852 Wang, S., Fast, J. D., Zheng, G., Jiang, J., Li, X., and Jiang, J. H.: Wintertime Particulate Matter



853 Decrease Buffered by Unfavorable Chemical Processes Despite Emissions Reductions in China,
854 *Geophys. Res. Lett.*, 47, 1–12, <https://doi.org/10.1029/2020GL087721>, 2020.

855 Li, B., Ma, Y., Zhou, Y., and Chai, E.: Research progress of different components of PM_{2.5} and
856 ischemic stroke, *Sci. Rep.*, 13, 1–12, <https://doi.org/10.1038/s41598-023-43119-5>, 2023.

857 Li, C., Martin, R. V, Shephard, M. W., Pereira, K. C., Cooper, M. J., Kaiser, J., Lee, C. J., Zhang,
858 L., and Henze, D. K.: Assessing the Iterative Finite Difference Mass Balance and 4D - Var Methods
859 to Derive Ammonia Emissions Over North America Using Synthetic Observations, *J. Geophys.*
860 *Res. Atmos.*, 124, 4222–4236, <https://doi.org/10.1029/2018JD030183>, 2019.

861 Li, L., Li, Q., Huang, L., Wang, Q., Zhu, A., Xu, J., Liu, Z., Li, H., Shi, L., Li, R., Azari, M., Wang,
862 Y., Zhang, X., Liu, Z., Zhu, Y., Zhang, K., Xue, S., Ooi, M. C. G., Zhang, D., and Chan, A.: Air
863 quality changes during the COVID-19 lockdown over the Yangtze River Delta Region: An insight
864 into the impact of human activity pattern changes on air pollution variation, *Sci. Total Environ.*,
865 732, <https://doi.org/10.1016/j.scitotenv.2020.139282>, 2020.

866 Lovarelli, D., Fugazza, D., Costantini, M., Conti, C., Diolaiuti, G., and Guarino, M.: Comparison of
867 ammonia air concentration before and during the spread of COVID-19 in Lombardy (Italy) using
868 ground-based and satellite data, *Atmos. Environ.*, 259, 118534,
869 <https://doi.org/10.1016/j.atmosenv.2021.118534>, 2021.

870 Malm, W. C.: Spatial and monthly trends in speciated fine particle concentration in the United
871 States, *J. Geophys. Res.*, 109, D03306, <https://doi.org/10.1029/2003JD003739>, 2004.

872 Matthias, V., Quante, M., Arndt, J. A., Badeke, R., Fink, L., Petrik, R., Feldner, J., Schwarzkopf,
873 D., Link, E. M., Ramacher, M. O. P., and Wedemann, R.: The role of emission reductions and the
874 meteorological situation for air quality improvements during the COVID-19 lockdown period in
875 central Europe, *Atmos. Chem. Phys.*, 21, 13931–13971, [https://doi.org/10.5194/acp-21-13931-](https://doi.org/10.5194/acp-21-13931-2021)
876 2021, 2021.

877 Mo, Z., Huang, J., Chen, Z., Zhou, B., Zhu, K., Liu, H., Mu, Y., Zhang, D., and Wang, S.: Cause
878 analysis of PM_{2.5} pollution during the COVID-19 lockdown in Nanning, China, *Sci. Rep.*, 11, 1–
879 13, <https://doi.org/10.1038/s41598-021-90617-5>, 2021.

880 Pai, S. J., Heald, C. L., and Murphy, J. G.: Exploring the Global Importance of Atmospheric
881 Ammonia Oxidation, *ACS Earth Sp. Chem.*, 5, 1674–1685,
882 <https://doi.org/10.1021/acsearthspacechem.1c00021>, 2021.

883 Patel, H., Talbot, N., Salmond, J., Dirks, K., Xie, S., and Davy, P.: Implications for air quality
884 management of changes in air quality during lockdown in Auckland (New Zealand) in response to
885 the 2020 SARS-CoV-2 epidemic, *Sci. Total Environ.*, 746, 141129,
886 <https://doi.org/10.1016/j.scitotenv.2020.141129>, 2020.

887 Paulot, F., Jacob, D. J., Pinder, R. W., Bash, J. O., Travis, K., and Henze, D. K.: Ammonia



888 emissions in the United States, European Union, and China derived by high-resolution inversion of
889 ammonium wet deposition data: Interpretation with a new agricultural emissions inventory
890 (MASAGE-NH₃), *J. Geophys. Res. Atmos.*, 119, 4343–4364,
891 <https://doi.org/10.1002/2013JD021130>, 2014.

892 Pisso, I., Sollum, E., Grythe, H., Kristiansen, N., Cassiani, M., Eckhardt, S., Arnold, D., Morton,
893 D., Thompson, R. L., Groot Zwaaftink, C. D., Evangeliou, N., Sodemann, H., Haimberger, L.,
894 Henne, S., Brunner, D., Burkhardt, J. F., Fouilloux, A., Brioude, J., Philipp, A., Seibert, P., and
895 Stohl, A.: The Lagrangian particle dispersion model FLEXPART version 10.4, *Geosci. Model Dev.*,
896 12, 4955–4997, <https://doi.org/10.5194/gmd-12-4955-2019>, 2019.

897 Pope, C. A. and Dockery, D. W.: Health effects of fine particulate air pollution: Lines that connect,
898 *J. Air Waste Manag. Assoc.*, 56, 709–742, <https://doi.org/10.1080/10473289.2006.10464485>, 2006.

899 Pope III, C. A., Burnett, R. T., Thun, M. J., Calle, E. E., Krewski, D., and Thurston, G. D.: Lung
900 Cancer, Cardiopulmonary Mortality, and Long-term Exposure to Fine Particulate Air Pollution, *J.*
901 *Am. Med. Assoc.*, 287, 1132–1141, <https://doi.org/10.1001/jama.287.9.1132>, 2002.

902 Pozzer, A., Tsimpidi, A. P., Karydis, V. A., De Meij, A., and Lelieveld, J.: Impact of agricultural
903 emission reductions on fine-particulate matter and public health, *Atmos. Chem. Phys.*, 17, 12813–
904 12826, <https://doi.org/10.5194/acp-17-12813-2017>, 2017.

905 Putaud, J. P., Pozzoli, L., Pisoni, E., Martins Dos Santos, S., Lagler, F., Lanzani, G., Dal Santo, U.,
906 and Colette, A.: Impacts of the COVID-19 lockdown on air pollution at regional and urban
907 background sites in northern Italy, *Atmos. Chem. Phys.*, 21, 7597–7609,
908 <https://doi.org/10.5194/acp-21-7597-2021>, 2021.

909 Putaud, J. P., Pisoni, E., Mangold, A., Hueglin, C., Sciare, J., Pikridas, M., Savvides, C., Ondracek,
910 J., Mbengue, S., Wiedensohler, A., Weinhold, K., Merkel, M., Poulain, L., Van Pinxteren, D.,
911 Herrmann, H., Massling, A., Nordstroem, C., Alastuey, A., Reche, C., Pérez, N., Castillo, S.,
912 Sorribas, M., Adame, J. A., Petaja, T., Lehtipalo, K., Niemi, J., Riffault, V., De Brito, J. F., Colette,
913 A., Favez, O., Petit, J. E., Gros, V., Gini, M. I., Vratolis, S., Eleftheriadis, K., Diapouli, E., Denier
914 Van Der Gon, H., Yttri, K. E., and Aas, W.: Impact of 2020 COVID-19 lockdowns on particulate
915 air pollution across Europe, *Atmos. Chem. Phys.*, 23, 10145–10161, <https://doi.org/10.5194/acp-23-10145-2023>, 2023.

917 Querol, X., Massagué, J., Alastuey, A., Moreno, T., Gangoiti, G., Mantilla, E., Duéguéz, J. J.,
918 Escudero, M., Monfort, E., Pérez García-Pando, C., Petetin, H., Jorba, O., Vázquez, V., de la Rosa,
919 J., Campos, A., Muñoz, M., Monge, S., Hervás, M., Javato, R., and Cornide, M. J.: Lessons from
920 the COVID-19 air pollution decrease in Spain: Now what?, *Sci. Total Environ.*, 779,
921 <https://doi.org/10.1016/j.scitotenv.2021.146380>, 2021.

922 Reche, C., Viana, M., Pandolfi, M., Alastuey, A., Moreno, T., Amato, F., Ripoll, A., and Querol,



- 923 X.: Urban NH₃ levels and sources in a Mediterranean environment, *Atmos. Environ.*, 57, 153–164,
924 <https://doi.org/10.1016/j.atmosenv.2012.04.021>, 2012.
- 925 Rennie, S., Watkins, J., Ball, L., Brown, M., Fry, M., Henrys, P., Hollaway, M., Quinn, J., Sier, A.,
926 and Dick, J.: Shaping the development of the UKCEH UK-SCAPE Data Science Framework.
927 Workshop report, 2020.
- 928 Rodgers, C. D.: *Inverse Methods for Atmospheric Sounding*, WORLD SCIENTIFIC, 256 pp.,
929 <https://doi.org/doi:10.1142/3171>, 2000.
- 930 Schobesberger, S., Franchin, A., Bianchi, F., Rondo, L., Duplissy, J., Kürten, A., Ortega, I. K.,
931 Metzger, A., Schnitzhofer, R., Almeida, J., Amorim, A., Dommen, J., Dunne, E. M., Ehn, M.,
932 Gagné, S., Ickes, L., Junninen, H., Hansel, A., Kerminen, V. M., Kirkby, J., Kupc, A., Laaksonen,
933 A., Lehtipalo, K., Mathot, S., Onnela, A., Petäjä, T., Riccobono, F., Santos, F. D., Sipilä, M., Tomé,
934 A., Tsagkogeorgas, G., Viisanen, Y., Wagner, P. E., Wimmer, D., Curtius, J., Donahue, N. M.,
935 Baltensperger, U., Kulmala, M., and Worsnop, D. R.: On the composition of ammonia-sulfuric-acid
936 ion clusters during aerosol particle formation, *Atmos. Chem. Phys.*, 15, 55–78,
937 <https://doi.org/10.5194/acp-15-55-2015>, 2015.
- 938 Seinfeld, J. H. and Pandis, S. N.: *Atmospheric Chemistry and Physics. From Air Pollution to*
939 *Climate Change*, 2nd ed., John Wiley & Sons, NY, 2000.
- 940 Shephard, M. W. and Cady-Pereira, K. E.: Cross-track Infrared Sounder (CrIS) satellite
941 observations of tropospheric ammonia, *Atmos. Meas. Tech.*, 8, 1323–1336,
942 <https://doi.org/10.5194/amt-8-1323-2015>, 2015.
- 943 Shephard, M. W., McLinden, C. A., Cady-Pereira, K. E., Luo, M., Moussa, S. G., Leithead, A.,
944 Liggio, J., Staebler, R. M., Akingunola, A., Makar, P., Lehr, P., Zhang, J., Henze, D. K., Millet, D.
945 B., Bash, J. O., Zhu, L., Wells, K. C., Capps, S. L., Chaliyakunnel, S., Gordon, M., Hayden, K.,
946 Brook, J. R., Wolde, M., and Li, S. M.: Tropospheric Emission Spectrometer (TES) satellite
947 observations of ammonia, methanol, formic acid, and carbon monoxide over the Canadian oil sands:
948 Validation and model evaluation, *Atmos. Meas. Tech.*, 8, 5189–5211, [https://doi.org/10.5194/amt-](https://doi.org/10.5194/amt-8-5189-2015)
949 [8-5189-2015](https://doi.org/10.5194/amt-8-5189-2015), 2015.
- 950 Shephard, M. W., Dammers, E., Cady-Pereira, K., Kharol, S., Thompson, J., Gainariu-Matz,
951 Y., Zhang, J., A. McLinden, C., Kovachik, A., Moran, M., Bittman, S., E. Sioris, C., Griffin, D., J.
952 Alvarado, M., Lonsdale, C., Savic-Jovicic, V., and Zheng, Q.: Ammonia measurements from space
953 with the Cross-track Infrared Sounder: Characteristics and applications, *Atmos. Chem. Phys.*, 20,
954 2277–2302, <https://doi.org/10.5194/acp-20-2277-2020>, 2020.
- 955 Shi, X. and Brasseur, G. P.: The Response in Air Quality to the Reduction of Chinese Economic
956 Activities During the COVID-19 Outbreak, *Geophys. Res. Lett.*, 47, 1–8,
957 <https://doi.org/10.1029/2020GL088070>, 2020.



958 Shi, Z., Song, C., Liu, B., Lu, G., Xu, J., Van Vu, T., Elliott, R. J. R., Li, W., Bloss, W. J., and
959 Harrison, R. M.: Abrupt but smaller than expected changes in surface air quality attributable to
960 COVID-19 lockdowns, *Sci. Adv.*, 7, <https://doi.org/10.1126/sciadv.abd6696>, 2021.

961 Sicard, P., De Marco, A., Agathokleous, E., Feng, Z., Xu, X., Paoletti, E., Rodriguez, J. J. D., and
962 Calatayud, V.: Amplified ozone pollution in cities during the COVID-19 lockdown, *Sci. Total
963 Environ.*, 735, <https://doi.org/10.1016/j.scitotenv.2020.139542>, 2020.

964 Sitwell, M., Shephard, M., Rochon, Y., Cady-Pereira, K., and Dammers, E.: An Ensemble-
965 Variational Inversion System for the Estimation of Ammonia Emissions using CrIS Satellite
966 Ammonia Retrievals, 22, 6595–6624, <https://doi.org/10.5194/acp-22-6595-2022>, 2022.

967 Sohrabi, C., Alsafi, Z., O'Neill, N., Khan, M., Kerwan, A., Al-Jabir, A., Iosifidis, C., and Agha, R.:
968 World Health Organization declares global emergency: A review of the 2019 novel coronavirus
969 (COVID-19), *Int. J. Surg.*, 76, 71–76, <https://doi.org/10.1016/j.ijisu.2020.02.034>, 2020.

970 Sørensen, L. L., Hertel, O., Skjøth, C. A., Lund, M., and Pedersen, B.: Fluxes of ammonia in the
971 coastal marine boundary layer, *Atmos. Environ.*, 37, 167–177, [https://doi.org/10.1016/S1352-
2310\(03\)00247-4](https://doi.org/10.1016/S1352-
972 2310(03)00247-4), 2003.

973 Stevens, C. J., Dupr, C., Dorland, E., Gaudnik, C., Gowing, D. J. G., Bleeker, A., Diekmann, M.,
974 Alard, D., Bobbink, R., Fowler, D., Corcket, E., Mountford, J. O., Vandvik, V., Aarrestad, P. A.,
975 Muller, S., and Dise, N. B.: Nitrogen deposition threatens species richness of grasslands across
976 Europe, *Environ. Pollut.*, 158, 2940–2945, <https://doi.org/10.1016/j.envpol.2010.06.006>, 2010.

977 Stohl, A., Forster, C., Frank, A., Seibert, P., and Wotawa, G.: Technical note: The Lagrangian
978 particle dispersion model FLEXPART version 6.2, *Atmos. Chem. Phys.*, 5, 2461–2474,
979 <https://doi.org/10.5194/acp-5-2461-2005>, 2005.

980 Sutton, M. A., Dragosits, U., Tang, Y. S., and Fowler, D.: Ammonia emissions from non-
981 agricultural sources in the UK, 34, 2000a.

982 Sutton, M. A., Dragosits, U., Tang, Y. S., and Fowler, D.: Ammonia emissions from non-
983 agricultural sources in the UK, *Atmos. Environ.*, 34, 855–869, 2000b.

984 Sutton, M. A., Erisman, J. W., Dentener, F., and Möller, D.: Ammonia in the environment: From
985 ancient times to the present, *Environ. Pollut.*, 156, 583–604,
986 <https://doi.org/10.1016/j.envpol.2008.03.013>, 2008.

987 Sutton, M. A., Reis, S., Riddick, S. N., Dragosits, U., Nemitz, E., Theobald, M. R., Tang, Y. S.,
988 Braban, C. F., Vieno, M., Dore, A. J., Mitchell, R. F., Wanless, S., Daunt, F., Fowler, D., Blackall,
989 T. D., Milford, C., Flechard, C. R., Loubet, B., Massad, R., Cellier, P., Personne, E., Coheur, P. F.,
990 Clarisse, L., Damme, M. Van, Ngadi, Y., Clerbaux, C., Skjøth, C. A., Geels, C., Hertel, O., Kruit,
991 R. J. W., Pinder, R. W., Bash, J. O., Walker, J. T., Simpson, D., Horvath, L., Misselbrook, T. H.,
992 Bleeker, A., Dentener, F., and Vries, W. de: Towards a climate-dependent paradigm of ammonia



993 emission and deposition, *Philos. Trans. R. Soc. B Biol. Sci.*, 368, 20130166–20130166,
994 <https://doi.org/10.1098/rstb.2013.0166>, 2013.

995 Szczepańska, A. and Pietrzyka, K.: The COVID-19 epidemic in Poland and its influence on the
996 quality of life of university students (young adults) in the context of restricted access to public
997 spaces, *J. Public Heal.*, <https://doi.org/10.1007/s10389-020-01456-z>, 2021.

998 Thunis, P., Clappier, A., Beekmann, M., Putaud, J. P., Cuvelier, C., Madrazo, J., and De Meij, A.:
999 Non-linear response of PM_{2.5} to changes in NO_x and NH₃ emissions in the Po basin (Italy):
1000 Consequences for air quality plans, *Atmos. Chem. Phys.*, 21, 9309–9327,
1001 <https://doi.org/10.5194/acp-21-9309-2021>, 2021.

1002 Tichý, O., Šmídl, V., Hofman, R., and Stohl, A.: LS-APC v1.0: A tuning-free method for the linear
1003 inverse problem and its application to source-Term determination, *Geosci. Model Dev.*, 9, 4297–
1004 4311, <https://doi.org/10.5194/gmd-9-4297-2016>, 2016.

1005 Tichý, O., Ulrych, L., Šmídl, V., Evangeliou, N., and Stohl, A.: On the tuning of atmospheric
1006 inverse methods: Comparisons with the European Tracer Experiment (ETEX) and Chernobyl
1007 datasets using the atmospheric transport model FLEXPART, *Geosci. Model Dev.*, 13, 5917–5934,
1008 <https://doi.org/10.5194/gmd-13-5917-2020>, 2020.

1009 Tichý, O., Eckhardt, S., Balkanski, Y., Hauglustaine, D., and Evangeliou, N.: Decreasing trends of
1010 ammonia emissions over Europe seen from remote sensing and inverse modelling, *Atmos. Chem.
1011 Phys.*, 23, 15235–15252, <https://doi.org/10.5194/acp-23-15235-2023>, 2023.

1012 Varotsos, C., Christodoulakis, J., Kouremadas, G. A., and Fotaki, E. F.: The Signature of the
1013 Coronavirus Lockdown in Air Pollution in Greece, *Water. Air. Soil Pollut.*, 232,
1014 <https://doi.org/10.1007/s11270-021-05055-w>, 2021.

1015 Viatte, C., Petit, J. E., Yamanouchi, S., Van Damme, M., Doucerain, C., Germain-Piaulenne, E.,
1016 Gros, V., Favez, O., Clarisse, L., Coheur, P. F., Strong, K., and Clerbaux, C.: Ammonia and pm_{2.5}
1017 air pollution in paris during the 2020 covid lockdown, *Atmosphere (Basel)*, 12, 1–18,
1018 <https://doi.org/10.3390/atmos12020160>, 2021.

1019 De Vries, W., Kros, J., Reinds, G. J., and Butterbach-Bahl, K.: Quantifying impacts of nitrogen use
1020 in European agriculture on global warming potential, *Curr. Opin. Environ. Sustain.*, 3, 291–302,
1021 <https://doi.org/10.1016/j.cosust.2011.08.009>, 2011.

1022 Wang, M., Xiao, M., Bertozzi, B., Marie, G., Rörup, B., Schulze, B., Bardakov, R., He, X. C., Shen,
1023 J., Scholz, W., Marten, R., Dada, L., Baalbaki, R., Lopez, B., Lamkaddam, H., Manninen, H. E.,
1024 Amorim, A., Ataei, F., Bogert, P., Brasseur, Z., Caudillo, L., De Menezes, L. P., Duplissy, J.,
1025 Ekman, A. M. L., Finkenzeller, H., Carracedo, L. G., Granzin, M., Guida, R., Heinritzi, M.,
1026 Hofbauer, V., Höhler, K., Korhonen, K., Krechmer, J. E., Kürten, A., Lehtipalo, K., Mahfouz, N. G.
1027 A., Makhmutov, V., Massabò, D., Mathot, S., Mauldin, R. L., Mentler, B., Müller, T., Onnela, A.,

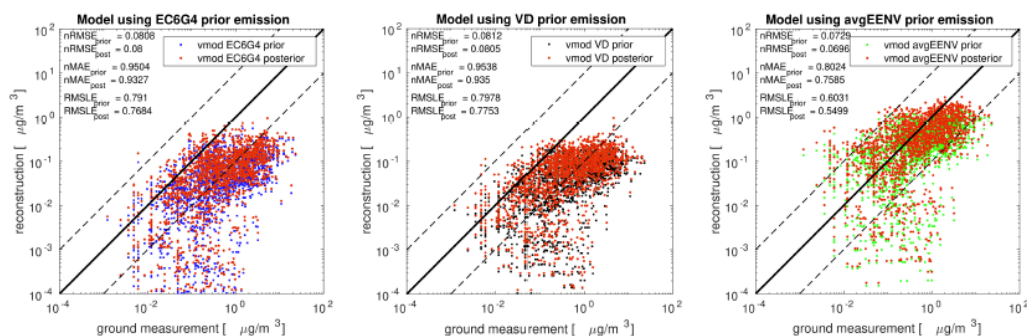


1028 Petäjä, T., Philippov, M., Piedehierro, A. A., Pozzer, A., Ranjithkumar, A., Schervish, M.,
1029 Schobesberger, S., Simon, M., Stozhkov, Y., Tomé, A., Umo, N. S., Vogel, F., Wagner, R., Wang,
1030 D. S., Weber, S. K., Welti, A., Wu, Y., Zauner-Wieczorek, M., Sipilä, M., Winkler, P. M., Hansel,
1031 A., Baltensperger, U., Kulmala, M., Flagan, R. C., Curtius, J., Riipinen, I., Gordon, H., Lelieveld,
1032 J., El-Haddad, I., Volkamer, R., Worsnop, D. R., Christoudias, T., Kirkby, J., Möhler, O., and
1033 Donahue, N. M.: Synergistic HNO₃–H₂SO₄–NH₃ upper tropospheric particle formation, *Nature*,
1034 605, 483–489, <https://doi.org/10.1038/s41586-022-04605-4>, 2022.
1035 Wang, P., Chen, K., Zhu, S., Wang, P., and Zhang, H.: Severe air pollution events not avoided by
1036 reduced anthropogenic activities during COVID-19 outbreak, *Resour. Conserv. Recycl.*, 158,
1037 104814, <https://doi.org/10.1016/j.resconrec.2020.104814>, 2020.
1038 Weber, R. J., McMurry, P. H., Mauldin, R. L., Tanner, D. J., Eisele, F. L., Clarke, A. D., and
1039 Kapustin, V. N.: New particle formation in the remote troposphere: A comparison of observations
1040 at various sites, *Geophys. Res. Lett.*, 26, 307–310, <https://doi.org/10.1029/1998GL900308>, 1999.
1041 Xu, W., Zhao, Y., Wen, Z., Chang, Y., Pan, Y., Sun, Y., and Ma, X.: Increasing importance of
1042 ammonia emission abatement in PM_{2.5} pollution control, *Sci. Bull.*, 67, 1745–1749,
1043 <https://doi.org/10.1016/j.scib.2022.07.021>, 2022.
1044 Zavyalov, V., Esplin, M., Scott, D., Esplin, B., Bingham, G., Hoffman, E., Lietzke, C., Predina, J.,
1045 Frain, R., Suwinski, L., Han, Y., Major, C., Graham, B., and Phillips, L.: Noise performance of the
1046 CrIS instrument, *J. Geophys. Res. Atmos.*, 118, 108–120, <https://doi.org/10.1002/2013JD020457>,
1047 2013.
1048 Zhai, S., Jacob, D. J., Wang, X., Liu, Z., Wen, T., Shah, V., Li, K., Moch, J. M., Bates, K. H., Song,
1049 S., Shen, L., Zhang, Y., Luo, G., Yu, F., Sun, Y., Wang, L., Qi, M., Tao, J., Gui, K., Xu, H., Zhang,
1050 Q., Zhao, T., Wang, Y., Lee, H. C., Choi, H., and Liao, H.: Control of particulate nitrate air
1051 pollution in China, *Nat. Geosci.*, 14, 389–395, <https://doi.org/10.1038/s41561-021-00726-z>, 2021.
1052 Zhang, X., Zhang, Z., Xiao, Z., Tang, G., Li, H., Gao, R., Dao, X., Wang, Y., and Wang, W.: Heavy
1053 haze pollution during the COVID-19 lockdown in the Beijing-Tianjin-Hebei region, China, *J.*
1054 *Environ. Sci. (China)*, 114, 170–178, <https://doi.org/10.1016/j.jes.2021.08.030>, 2022.
1055 Zhang, Y., Zhang, C., Liu, Z., and Yang, X.: Air pollution reduction during COVID-19 lockdown
1056 in China: a sustainable impact assessment for future cities development, *City Built Environ.*, 1, 1–
1057 21, <https://doi.org/10.1007/s44213-023-00013-0>, 2023.
1058
1059



1060 **FIGURE LEGENDS**

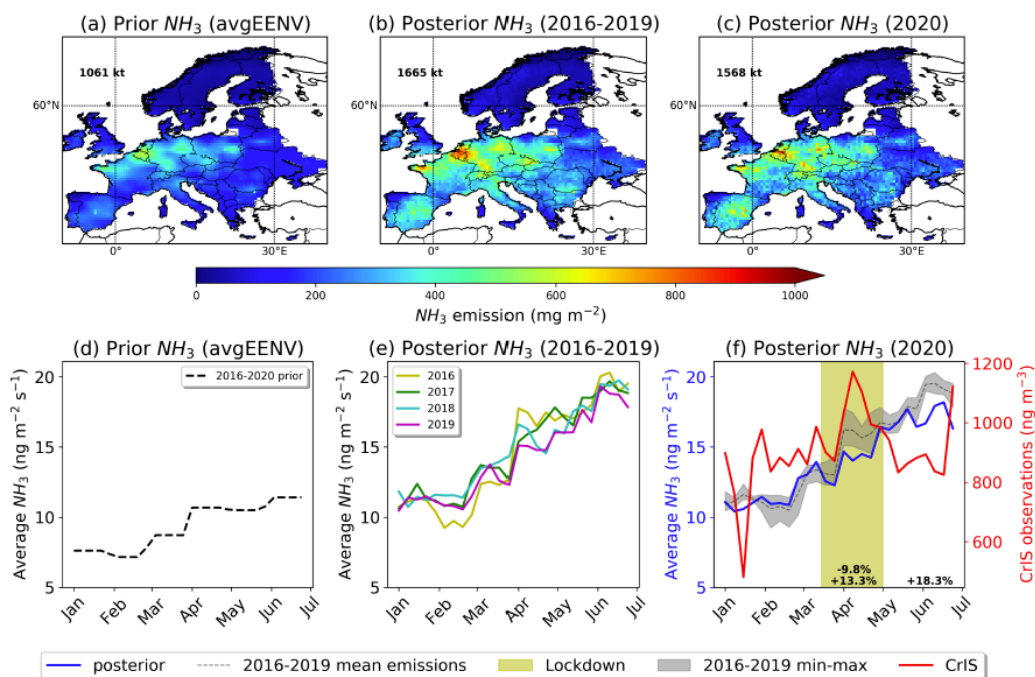
1061



1062

1063 **Figure 1.** Scatter plots of prior and posterior concentrations against independent observations
1064 (observations that were not included in the inversion algorithm) from the EMEP network
1065 (<https://emep.int/mscw/>, **Error! Reference source not found.**) from January to July 2020. Three
1066 statistical measures (nRMSE, nMAE and RMSLE) were used to assess the performance of each
1067 inversion using three different prior emission inventories for ammonia (EC6G4, VD and
1068 avgEENV).

1069

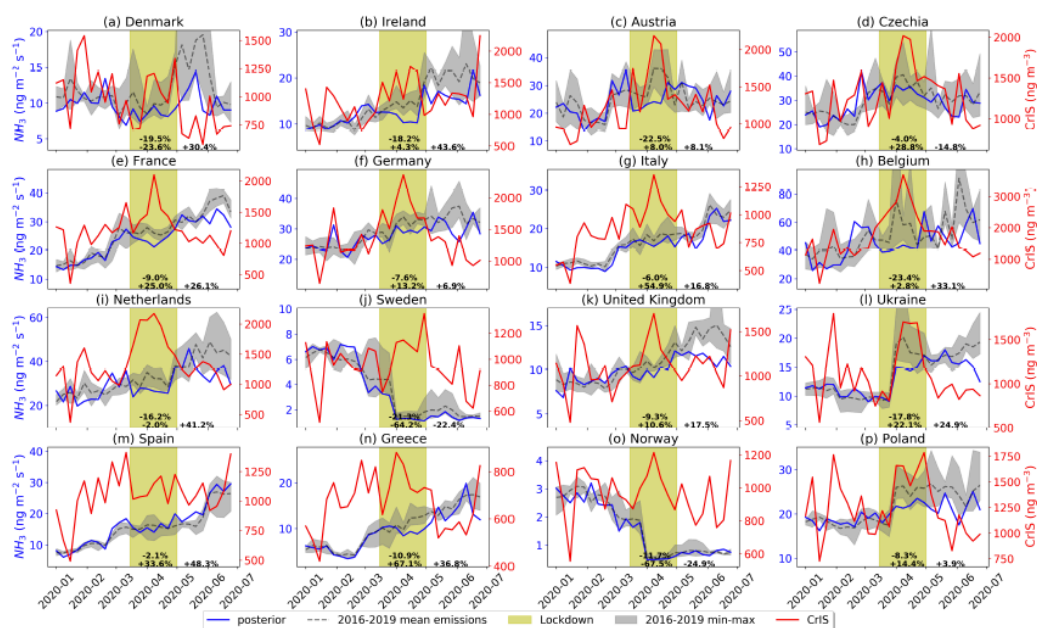


1070

1071 **Figure 2.** (a) Total a priori emissions of ammonia over Europe for the inversion period (January –
 1072 June). The emissions correspond to avgEENV prior, and the total emitted amount is equal to 1061 kt.
 1073 (b) Total a posteriori emissions of ammonia over Europe for the inversion period (January – June)
 1074 for the reference period 2016 – 2019 (using avgEENV prior) that amount 1665 kt. (c) Total posterior
 1075 emissions of ammonia over Europe for January – June 2020 (1568 kt) using the avgEENV as the
 1076 prior. (d) Timeseries of weekly-average prior emissions of ammonia over Europe (January to June
 1077 2020) from avgEENV prior. (e) Timeseries of weekly-average posterior emissions of ammonia over
 1078 Europe for the reference years 2016–2019 (January to June) (yellow, green, cyan, magenta colors).
 1079 (f) Timeseries of weekly-average posterior emissions of ammonia over Europe in 2020 resulting from
 1080 inversions using the avgEENV prior are plotted together with the CrIS observations averaged over
 1081 Europe (red line) and minimum, mean and maximum ammonia emissions in the reference period
 1082 (2016–2019). The single top number -9.8% shows percentage change in ammonia emissions during
 1083 the 2020 lockdown as compared to the same period in reference years, whereas two bottom ones show
 1084 the corresponding changes in ammonia emissions (i) during the 2020 lockdown as compared to the
 1085 period before lockdown (+13.3%), and (ii) the period after lockdown finished as compared to the
 1086 lockdown period +18.3%), known as rebound period.

1087

1088

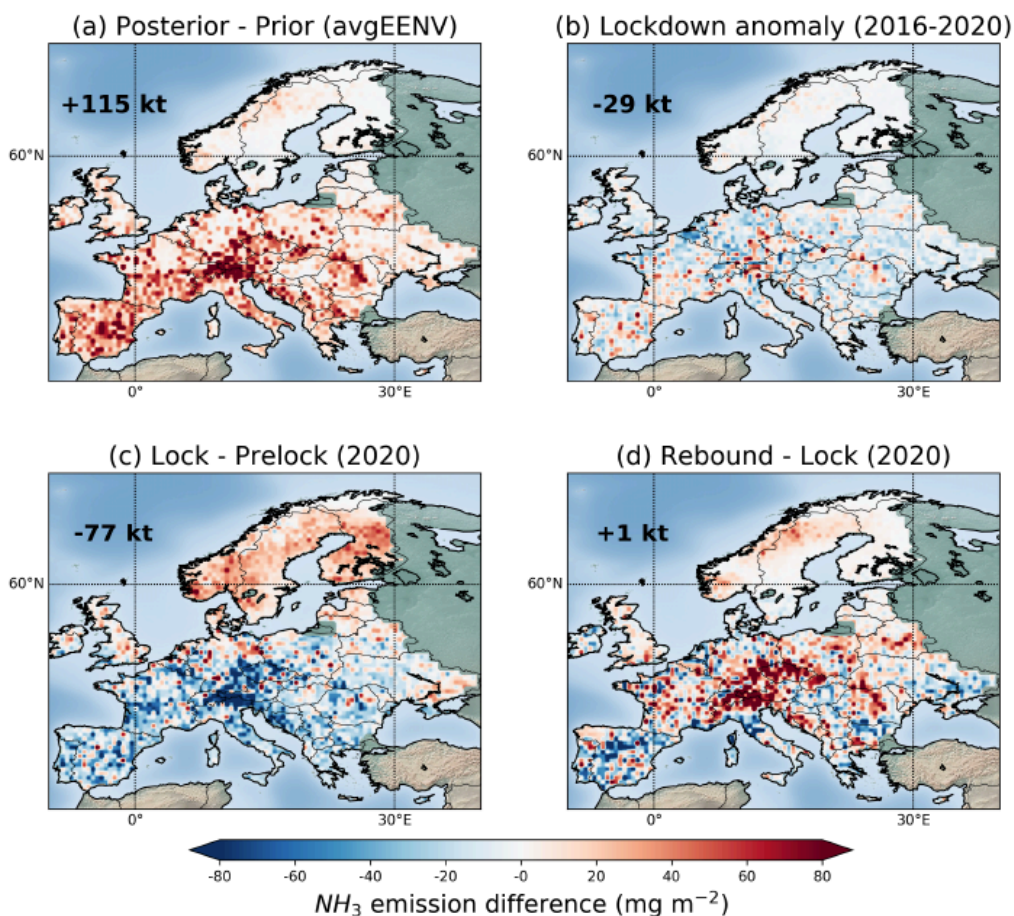


1089

1090 **Figure 3.** Timeseries of weekly-average posterior emissions of ammonia in different European
1091 countries in 2020 resulting from inversions using prior information from avgEENV plotted together
1092 with the CrIS observations averaged over Europe (red line) and minimum, mean and maximum
1093 ammonia emissions for the reference period (2016–2019). The single top numbers show the change
1094 in ammonia emissions during the 2020 lockdowns (15 March – 30 April) as compared to the same
1095 period the years before (2016–2019), whereas the two bottom ones show the respective changes in
1096 ammonia emissions during the 2020 lockdown as compared to the period before the lockdown, and
1097 after lockdown finished compared to the lockdown period (rebound period).

1098

1099

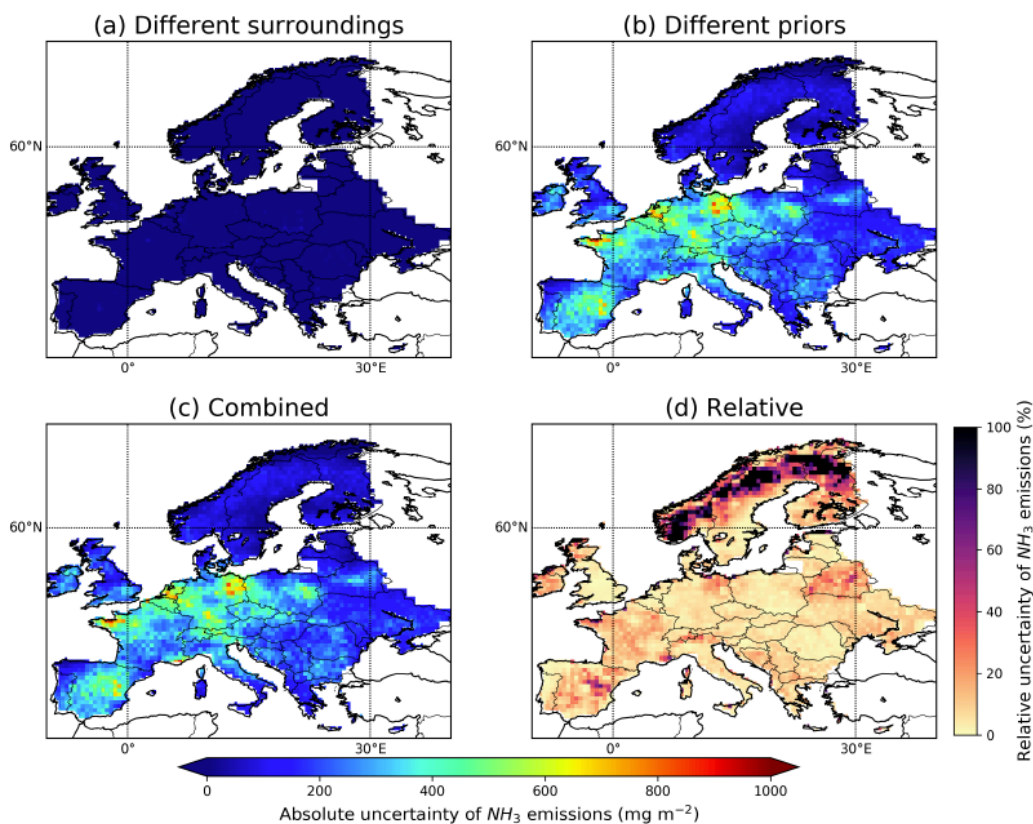


1100

1101 **Figure 4.** (a) Difference of posterior from prior emissions of ammonia during the European
1102 lockdowns of 2020 (15 March – 30 April) using the avgEENV emissions as the prior. (b) Emission
1103 anomaly relative to the 2020 lockdowns from the 2016-2020 period (15 March – 30 April).
1104 Difference in posterior ammonia (c) during the 2020 lockdowns (15 March – 30 April, Lock) from
1105 the period before (1 January – 14 March) and (d) after the 2020 lockdowns (1 May – 31 June, Reb)
1106 from the period during the 2020 lockdowns (15 March – 30 April, Lock) compared with the
1107 reference years (2016–2019).

1108

1109

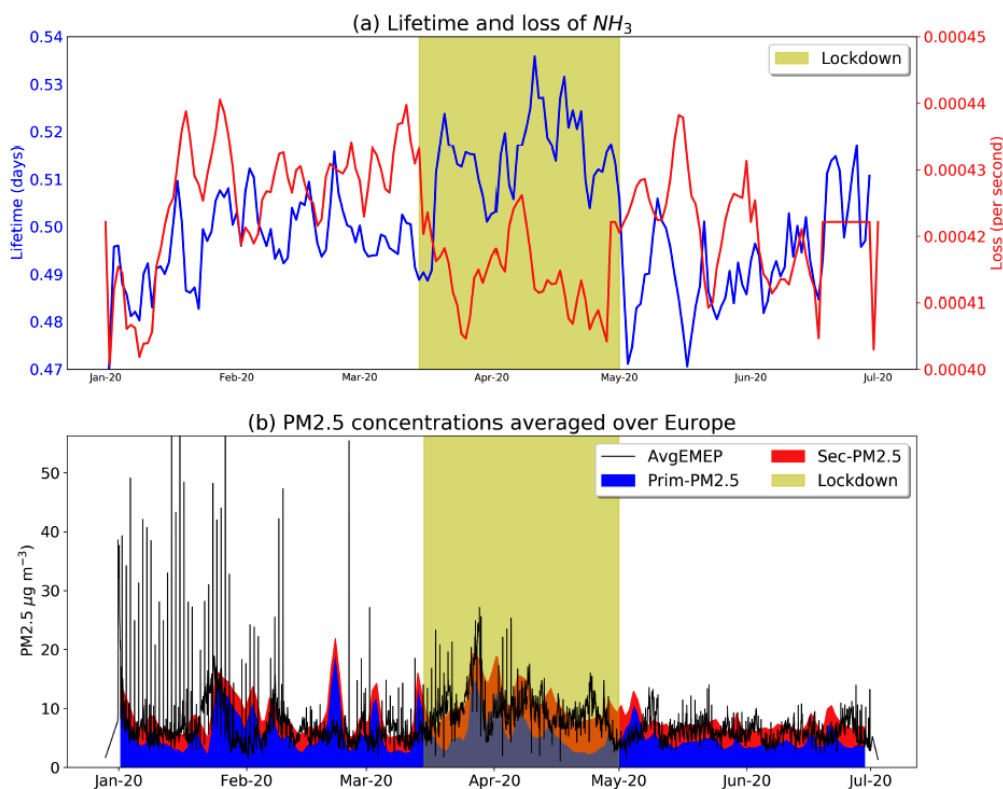


1110

1111 **Figure 5.** (a) Absolute uncertainty from use of different surrounding grid area for each spatial
1112 element of our inversion domain in the sensitivity tests; 2° to 4° grid-cells were considered resulting
1113 in a mean relative uncertainty of 4%. (b) Absolute uncertainty from use of four different prior
1114 emission estimates, namely EC6G4, VD, EGG and NE (see section 2.3). Here, a much larger
1115 uncertainty was calculated, due to the use of tenfold different prior emission datasets. (c)
1116 Propagated absolute uncertainty from the different sensitivity tests, and (d) relative uncertainty with
1117 respect to the posterior emissions (**Figure 2c**). The average uncertainty in the inversion domain for
1118 the first half of 2020 was estimated to be 48%.

1119

1120



1121

1122 **Figure 6.** (a) Modelled lifetime (blue) and loss-rates (red) of atmospheric ammonia averaged over
1123 Europe for January – June 2020. The lockdown period (15 March – 30 April) is shaded in yellow.
1124 Right after COVID-19 restrictions were applied, loss-rates of ammonia (shown in red) were
1125 disturbed due to reported decreases on SO_2 and NO_x (Guevara et al., 2021; Doumbia et al., 2021),
1126 precursors of sulfuric and nitric acids (with which ammonia reacts to form PM_{2.5}) and the constant
1127 accumulation of atmospheric ammonia. This had an effect on the lifetime of ammonia (plotted in
1128 blue), which started increasing in Europe leading to further accumulation of ammonia. (b)
1129 Observations of PM_{2.5} from the EMEP stations (78 stations) plotted against modelled PM_{2.5}
1130 concentrations, both averaged over Europe, from primary sources and secondary formation. It is
1131 evident that right after lockdown (yellow shade), secondary PM_{2.5} formation maintained high
1132 concentrations across Europe.

1133